Carbohydrate Polymers 323 (2024) 121418

Contents lists available at ScienceDirect

Carbohydrate Polymers

journal homepage: www.elsevier.com/locate/carbpol

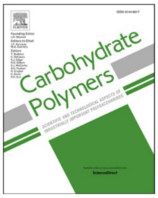

Magnetically-activated, nanostructured cellulose for efficient capture of circulating tumor cells from the blood sample of head and neck cancer patients

Raj Shankar Hazra [a,b,1], Narendra Kale [b,c], Camden Boyle [d], Kayla B. Molina [e,2], Alain D'Souza [f,j], Gourishankar Aland [f,j], Long Jiang [a,1], Pankaj Chaturvedi [g], Santaneel Ghosh [d], Sanku Mallik [c], Jayant Khandare [f,h,i,j,*], Mohiuddin Quadir [b,1,**]

[a] *Department of Mechanical Engineering, North Dakota State University, Fargo, ND 58108, USA*
[b] *Department of Coatings and Polymeric Materials, North Dakota State University, Fargo 58108, ND, USA*
[c] *Department of Pharmaceutical Sciences, North Dakota State University, Fargo 58108, ND, USA*
[d] *Department of Engineering and Technology, Southeast Missouri State University, One University Plaza, MS6825, Cape Girardeau, MO 63701, USA*
[e] *Department of Biomedical Engineering, The University of Minnesota Twin Cities, Minneapolis, MN 55455, USA*
[f] *Actorius Innovations and Research, Pune, India*
[g] *Department of Head and Neck Surgical Oncology, Tata Memorial Hospital, Mumbai, India*
[h] *School of Pharmacy, Dr. Vishwananth Karad MIT World Peace University, Pune 411038, India*
[i] *School of Consciousness, Dr. Vishwananth Karad MIT World Peace University, Pune 411038, India*
[j] *Actorius Innovations and Research, Simi Valley, CA 93063, USA*

ARTICLE INFO

Keywords:
Cellulose nanofiber
Cellulose nanocrystal
Nanostructures
Circulating tumor cells
Cancer

ABSTRACT

In this report, the relative efficiency of cellulose nanocrystals (CNCs) and nanofibers (CNFs) to capture circulating tumor cells (CTCs) from the blood sample of head and neck cancer (HNC) patients was evaluated. Detection and enumeration of CTCs are critical for monitoring cancer progression. Both types of nanostructured cellulose were chemically modified with Epithelial Cell Adhesion Molecule (EpCAM) antibody and iron oxide nanoparticles. The EpCAM antibody facilitated the engagement of CTCs, promoting entrapment within the cellulose cage structure. Iron oxide nanoparticles, on the other hand, rendered the cages activatable via the use of a magnet for the capture and separation of entrapped CTCs. The efficiency of the network structures is shown in head and neck cancer (HNC) patients' blood samples. It was observed that the degree of chemical functionalization of hydroxyl groups located within the CNCs or CNFs with anti-EpCAM determined the efficiency of the system's interaction with CTCs. Further, our result indicated that inflexible scaffolds of nanocrystals interacted more efficiently with CTCs than that of the fibrous CNF scaffolds. Network structures derived from CNCs demonstrated comparable CTC capturing efficiency to commercial standard, OncoDiscover®. The output of the work will provide the chemical design principles of cellulosic materials intended for constructing affordable platforms for monitoring cancer progression in 'real time'.

1. Introduction

Cellulose-based nanomaterials are a rich repertoire of biopolymers obtained from renewable resources. These nanoscale materials exhibit unique physico-chemical properties, such as biocompatibility, biodegradability, and environmental sustainability, and have opened numerous avenues in the area of diagnostics and biomolecular separation (Abdul Khalil et al., 2020; Calvino et al., 2020; Czaja et al., 2007; Domingues et al., 2014; Gatenholm & Klemm, 2010; Hazra et al., 2020; Hazra et al., 2022; Hickey & Pelling, 2019; Jorfi & Foster, 2015; Joseph

---

* Correspondence to: J. Khandare, School of Pharmacy, Dr. Vishwananth Karad MIT World Peace University, Pune 411038, India.
** Correspondence to: M. Quadir, Department of Coatings and Polymeric Materials, North Dakota State University, Fargo 58108, ND, USA.
E-mail addresses: jayant@actorius.co.in (J. Khandare), mohiuddin.quadir@ndsu.edu (M. Quadir).

[1] Materials and Nanotechnology Program, North Dakota State University, Fargo, ND 58108, USA.

[2] Current affiliation: Department of Biomedical Engineering, The University of Minnesota Twin Cities, Minneapolis, MN 55455, USA

https://doi.org/10.1016/j.carbpol.2023.121418
Received 26 September 2022; Received in revised form 14 September 2023; Accepted 18 September 2023

et al., 2020; Picheth et al., 2017; Rakib Hasan Khan et al., 2022; Unal et al., 2020). There are two main types of cellulosic nanostructures – cellulose nanocrystals (CNCs) and nanofibers (CNFs) (Hazwan Hussin et al., 2019; Pennells et al., 2020; Trache et al., 2016; Trache et al., 2020). The advantages of these nanomaterials are their relatively high aspect ratio and specific surface area, multivalency properties, large number of reactive surface functional groups, ease of purification post-manufacturing, better dispersibility in polar solvents, biocompatibility, and non-toxicity (Hazra et al., 2020; Incani et al., 2013). For example, numerous hydroxyl groups on the surface of cellulose nanomaterials can be easily modified using facile and orthogonal chemical conjugation techniques, such as esterification, etherification, and conversion into 'clickable' reactive groups such as azides, alkynes, or thiols. The regular spacing of these functional groups on cellulosic backbone thus provides tunable flexibility, superior mechanical properties, electrical conductivity, steric selectivity, and affinity towards other biomolecules in a multivalent fashion (Hazra et al., 2021; Jia et al., 2019; Ma et al., 2021; Rose & Palkovits, 2011). Further, cellulosic materials can be easily purified following a chemical reaction, are easily dispersed in multiple hydrophilic media, and have biocompatibility with numerous biological components, resulting in non-toxicity (Hazra et al., 2020; Incani et al., 2013). Thus, cellulose nanomaterials have been utilized as an excellent platform for preparing optical and enzymatic biosensors with a non-sticky, carbohydrate-rich surface that promotes specificity with a target analyte while inhibiting engagement with the non-targeted ones (Incani et al., 2013).

The central hypothesis of this work is based on the idea that cellulose nanostructures and its structure-property-aspect ratio relationship govern their interactions with other synthetic and biological materials of interest (Edwards et al., 2013; Golmohammadi et al., 2017; Hazra et al., 2020; Lam et al., 2012). To prove this hypothesis, we investigated the effect of both types of cellulose nanostructures, i.e., CNCs and CNFs, on their interactions with a clinically-relevant biological entity, such as Circulating Tumor Cells (CTCs) of the head and neck cancer (HNC). Detection, isolation, and enumeration of CTCs in HNC are critical for monitoring cancer progression and determining therapeutic success (Buglione et al., 2012; He et al., 2013; Kawada et al., 2017; Kulasinghe et al., 2015; Kulasinghe et al., 2016; Kulasinghe et al., 2017; Kulasinghe et al., 2018; Kulasinghe, Hughes, et al., 2019; Kulasinghe, Zhou et al., 2019; McMullen Kyle et al., 2016; Nichols et al., 2012; Tada et al., 2020; Tinhofer & Staudte, 2018; Zheng et al., 2019). As a target of clinical importance, CTCs are extremely valuable because they directly relate to metastasis. Metastasis is one of the leading causes of cancer-related deaths world-wide. Approximately 10 million people die from cancer annually, and 90 % of these cases are associated either with treatment failure or metastasis (Chaffer & Weinberg, 2011; Sung et al., 2021). Correlating the treatment stage and the presence of CTCs in circulation will reduce the chances of disseminating tumor cells and progression to secondary tumors in HNCs (Necula et al., 2019). However, detection of CTCs in peripheral blood is extremely challenging as the concentration of CTCs is very low, i.e., <0.1 % in peripheral blood (Cristofanilli et al., 2004). Due to various physiological factors, such as shear stress of blood flow and immune activity, most CTCs show a limited half-life ranging between 1.0 and 2.4 h (Hu et al., 2021; Meng et al., 2004; Tayoun et al., 2019). Thus, developing the CTC-capture and enrichment platform is challenging owing to such short half-life and low abundance of CTC, non-specificity, low binding efficiency, and patient-to-patient variation (Singh et al., 2021). Thus, multi-pronged approaches have been reported across the literature to develop an efficient and affordable CTC detection platform. Microfluidic chips, for example, are one of the approaches used extensively for capturing CTC with significant CTC capture efficiency, ranging from 65 to 95 % (Gleghorn et al., 2010; Hsiao et al., 2014; Kulasinghe, Zhou et al., 2019; Nagrath et al., 2007; Wu et al., 2019; Yoon et al., 2016). These microfluidic platforms are decorated with microposts array grafted with anti-EpCAM or Transferrin (Tf) glycoproteins. The microfluidic system developed by Chen et al. captured CTCs from HCT116 cell line with 85 % capture efficiency (Chen et al., 2019). Zhu et al. developed a hierarchical hydrogel system-based microfluidic chip used as a liver cancer-on-a-chip and drug screening device (Zhu et al., 2021). Zheng et al. fabricated aptamer-functionalized barcode particles for capturing CTCs (Zheng et al., 2014). Similarly, Luan et al. developed folic Acid-conjugated photonic barcodes for detecting and capturing CTCs (Luan et al., 2018). Droplet microfluidic systems developed by Liu et al. used bubble-propelled nanomotors (Liu et al., 2022) and have been harnessed for capturing CTCs. These systems can be used for capturing CTCs by grafting specific protein molecules. Dielectrophoretic and magnetophoretic microfluidic chips have also been designed and were used to capture CTCs from blood flow (Zhao et al., 2022). Using CNF based microfluidic system, Kumar et al. successfully captured CTCs from HCT116 cancer cell line using Anti-EpCAM on the surface of channel (Kumar et al., 2020). A few of the challenges of microfluidic channels are reduction in capturing efficiency due to high flow rate, low contact time with the channel, and low contact point for large volume blood (Nagrath et al., 2007; Schulz et al., 2009; Shen et al., 2017). Therefore, membrane microfilter-based systems were used to capture CTCs by flowing blood sample through pores of these filters. As representative example, Khetani et al. developed a membrane-based filter system to isolate CTCs from blood flow (Khetani et al., 2018). Similarly, Boya et al. fabricated meshed microwells to capture CTC clusters from prostate and ovarian cancer patients at a throughput of >25 mL/h (Boya et al., 2022). Membrane-based filter systems also exhibit some challenges, including but not limited to the clogging of the pores located within the membranes (Adams et al., 2014; Lee et al., 2019; Zheng et al., 2011). Another technique for isolating CTC from blood samples used functionalized silica-based microbeads (Sun et al., 2018; Yoo et al., 2016). Major drawbacks of this method involved precise detection of CTCs (due to the involvement of free microbeads mixed in the system) and interference with fluorescence-based detection methods due to light diffraction within free microbeads (Xu, 2001; Yoo et al., 2016). Immunochemistry-based techniques, such as those developed by CellSearch and MagSweeper, gained clinical acceptance and popularity (Talasaz et al., 2006; Talasaz et al., 2009). MagSweeper can isolate CTCs from blood at a maximum of 62 % capture efficiency with EpCAM biomarker (Deng et al., 2014; Xiong et al., 2016). Li et al. developed an immunomagnetic system to capture CTCs with 89–91 % capture efficiency (Li et al., 2022). Similarly, Jiang et al. designed protein corona-coated immunomagnetic nanoparticles to capture CTCs with 90 % efficiency (Jiang et al., 2022). Recently, the Strep-tag® showed CTC capturing efficiency of 79 % with EpCAM, HER2, EGFR biomarkers under external magnetic field (Lu et al., 2015). CTC capturing efficiency of a detection platform increased significantly when fiber-type materials with large surface area and multiple functional groups were used. For capturing CTC efficiently, Tseng et al. demonstrated the importance of nanofibers in the form of electrospun mat prepared by blending poly (sulfobetaine methacrylate) (PSBMA) and poly (acrylic acid) (PAA) into nylon-6 (Tseng et al., 2016). Similarly, Lee et al. developed a mat-based CTC assay by blending poly(ethylene oxide) (PEO) and nylon-6 fibers via electrospinning method (Lee et al., 2018). In recent cases, poly(amidoamine) (PAMAM) dendrimers were functionalized with CTC responsive protein molecules to isolate CTCs from blood by exploring multivalency properties (Bu et al., 2020; Meng et al., 2020; Myung et al., 2011; Myung et al., 2015). Based on these previous reports, this is apparent that network like structures with multiple functional groups, multivalency and tunable physico-chemical properties provide augmented efficiency for capturing CTC (Myung et al., 2012; Zhang & King, 2017). Thus, in the current project, we designed a CTC capture platform using CNC and CNF that form network structures and investigated how their nanoscale properties impact the capture efficiency of CTCs from patient blood. To achieve this, the native hydroxyl functional groups on CNCs and CNFs were first converted to amines, and then chemically modified to thiol to coordinate with iron oxide nanoparticles (Fe_3O_4 NPs). The resulting cellulosic product was chemically conjugated with anti-EpCAM. This particular class of antibody was selected because cancer cells consume a higher amount of iron and other essential minerals than that of healthy cells for survival. These nutrients are transported across the membrane via transmembrane glycoproteins, such as Transferrin (Tf) and epithelial cell adhesion molecule (EpCAM) receptor (Gomme et al., 2005; Han et al., 2010; Zhang et al., 2017). Superparamagnetic Fe_3O_4 NPs were used to render the scaffold magnetically separable post-interaction with anti-EpCAM-engaging cells. In this study, functionalized products after each chemical modification step were characterized with X-ray photoelectron spectroscopy (XPS) and Fourier Transform Infrared Spectrometer (FTIR) spectroscopy. The assembly structure of chemically modified CNCs or CNFs was evaluated using Transmission electron microscopy (TEM), Dynamic light scattering (DLS), and Zeta (ζ-) potential measurement. Magnetic measurement with Vibrating Sample Magnetometer (VSM) was carried out to investigate the effect of temperature on the magnetic properties of CNC and CNF scaffolds. CTC capture efficiency was investigated on the human colon cancer cell line (HCT116) and head and neck cancer cell lines. This capture efficiency was compared with the commercial standard, OncoDiscover®. We envision that this work will shed light on the design principles required for constructing magnetically activable, CTC-capturing scaffolds with cellulosic nanomaterials and deconvolute the effect of aspect ratio, and flexibility of scaffolds on their efficiency in capturing CTCs from cancer patients' blood. The working principle of the cellulosic nano-scaffold and its CTC capture mechanism is illustrated in Fig. 1.

2. Experiment section

2.1. Materials and methods

Freeze-dried cellulose nanocrystals (CNCs) powder (1 wt% sulfur and sodium form) was purchased from the Process Development center of the University of Maine. CNCs were collected from biomass. Extraction processes involved hydrolysis of the biomass with sulfuric acid (Postek et al., 2013; Wang et al., 2020). The amorphous part of cellulose nanofibers was dissolved with acid treatment, yielding a highly crystalline fraction of the nanofiber, which is 3–20 nm wide and 150–200 nm long. These rod-like nanocrystals (Also known as cellulose nanowhiskers) (Hazra et al., 2020) showed high axial stiffness (~150 GPa), tensile strength (~7.5 GPa), thermal stability (~300 °C), superior aspect ratio (10−100), and low density (~1.6 g/cm^3) (Postek et al., 2013). Cellulose nanofibrils (CNFs) were purchased as 3 wt% aqueous slurries from the Process Development center of the University of Maine. This slurry was produced using circulating bleached softwood pulp over a specialized refiner without any pre- or chemical treatment (Fein et al., 2020; Ma et al., 2021; Wang et al., 2020). The specific surface area and density of CNFs were 31–33 m^2/g and 1.0 g/cm^3, respectively. Nanofibers used in this study were 50 nm wide and micron-scale long (Chen et al., 2020; Li, Skolrood, et al., 2019). Other reagents and chemicals, such as ferric chloride hexahydrate, ferrous chloride tetrahydrate (CAS 13478-10-9), fluorescein isothiocyanate (CAS 27072-45-3), and Traut's Reagent (CAS 4781-83-3) were procured from Sigma Aldrich. Anti-EpCAM antibody (ab71916) was purchased from Abcam. A 28 % ammonium hydroxide was purchased from Sigma Aldrich (CAS 1336-21-6).

2.2. Synthesis of iron oxide nanoparticles (Fe_3O_4 NPs)

Iron oxide nanoparticles were synthesized following slight modification of previously published procedure (Banerjee & Chen, 2007). Prior to the modification of CNCs and CNFs, iron oxide nanoparticles (Fe_3O_4) were precipitated from 30 mL, 1:1 (v/v) liquid mixture of Ferrous chloride tetrahydrate (0.1 M solution, 0.19 g solid dissolved in 15 mL DI water) and Ferric Chloride, hexahydrate (0.2 M solution, 0.487 g solid dissolved in 15 mL DI water) followed by addition of 28 % concentrated NH_4OH in a dropwise fashion to reach a pH of 10. Such elevation of pH resulted in the precipitation of Fe_3O_4 NPs. Precipitated NPs were heated at 80 °C for 30 min. A dark reddish-brown sample was washed by centrifugation with ethanol and DI water. We have used 50 mL centrifuge tubes and centrifuged at 10000 rpm (10,304 ×g) for 10 min. This allowed to precipitate the nanocrystal to form a pallet in the bottom of the centrifuge tube.

2.3. Conjugation of Fe_3O_4 NPs with CNC or CNFs to form network structures

Modification of CNCs and CNFs to conjugate Fe_3O_4 NPs was

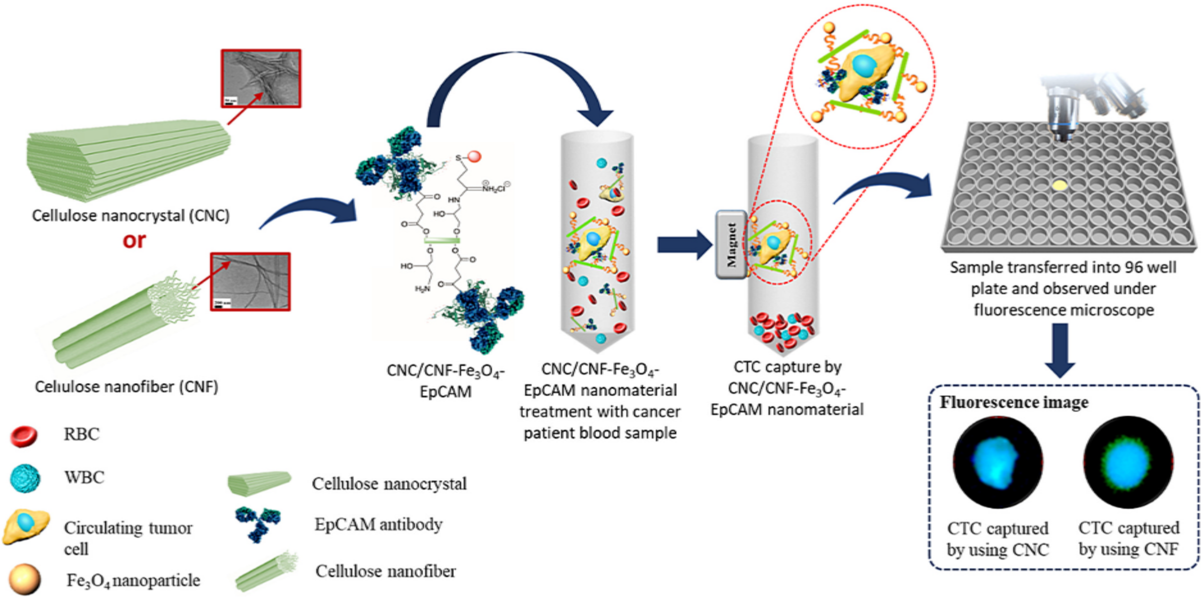

Fig. 1. Schematic diagram of anti-EpCAM decorated and Fe_3O_4 NP conjugated CNC- and CNF-based network structures. In the inset, TEM images are shown representing the structural difference between CNC and CNF scaffold. Schematic illustration showing the process of CTC isolation from blood sample containing RBC, WBC, platelets, and CTCs. The sample was collected from HNC patients ($n = 6$). Strong magnet was used for CTC separation.

conducted in multiple steps following earlier protocol (Fig. 2) (Hazra et al., 2020). A dispersibility test was conducted earlier to identify the solvent system and cellulose concentration range where cellulose does not precipitate out from the aqueous suspension (Supporting information, Fig. S1, and Table S1). Then, 1 g of CNCs or CNFs were dispersed in 22 mL sodium hydroxide solution (1 M), followed by the addition of varying concentrations of epichlorohydrin (48, 96, 144, and 196 mmol/g of cellulose). The reaction mixture was incubated at 60 °C for 2 h and dialyzed against deionized water (Repligen, Spectra/Por 3 Dialysis Tubing, 3.5 kD MWCO) until pH was below 12. After completion of this step, centrifugation of the reaction mixture at 10,000 rpm (50 mL centrifuge tube, 10,304 ×*g*) for 10 min was carried out to separate the desired product at >97 % yield. Then, 28 % ammonium hydroxide (2.5 mL/g cellulose) was added to the product (adjusted pH at 12), and the mixture was incubated for an additional 2 h at 60 °C with constant stirring. After the stipulated reaction period, the sample was again centrifuged at 10,000 rpm (50 mL centrifuge tube, 10,304 ×*g*) for 10 min to discard unreacted ammonium hydroxide. The centrifuged product was dialyzed against deionized water (Repligen, Spectra/Por 3 Dialysis Tubing, 3.5 kD MWCO) until pH reached ~7 (Final yield of the product was >95 %). Following the amination step of CNCs or CNFs, Traut's reagent (Fig. 2) was added to the modified amino-functionalized cellulosic products. To carry out this reaction, a coupling buffer was first prepared by dissolving 73 mg ethylenediamine tetra acetic acid (EDTA) in 50 mL phosphate-buffered saline (PBS). The pH of the coupling buffer was adjusted to 7.6. Amine functionalized CNCs and CNFs (8 mg) were dispersed in the coupling buffer (950 μL) and reacted with Traut's reagent (2-iminothiolane) (50 μL from a mother solution prepared via dissolving 2 mg Traut's reagent in 1 mL coupling buffer) for 45 min incubation at room temperature. The final sample was centrifuged at 10,000 rpm (50 mL centrifuge tube, 10,304 ×*g*) for 10 min and washed with deionized water to obtain thiolated CNCs and CNFs (Yield > 96 %). Previously prepared Fe_3O_4 NPs dispersed in water (pH 10) were immediately added to this thiolated CNC (8 mg/mL) or CNF (12 mg/mL) suspension solution in a varied amounts (10, 12, 15, 18, 20, and 40 mg/mL) to obtain magnetically activable CNC or CNF networks. The final conjugated product was washed with centrifugation (50 mL centrifuge tube, 10,304 ×*g*) to remove unconjugated Fe_3O_4 NPs. The quantification of conjugated Fe_3O_4 NPs was evaluated using a calibration curve via UV–Vis spectroscopic analysis at 370 nm (Hazra et al., 2020).

2.4. *Introduction of carboxyl group on network structures via succinylation and conjugation of anti-EpCAM*

Carboxylic acid groups were introduced on CNC or CNF scaffolds via succinylation reaction (Fischer et al., 2011). Introducing these carboxylic acid groups allowed further modification of the CNC or CNF scaffolds with epithelial cell adhesion molecule (anti-EpCAM) via an amidation reaction (Fig. 2). For this reaction, a dispersion of amino-functionalized, nanoparticle-conjugated CNC or CNF (1.0 g) network structures in dimethylformamide (DMF, 15 mL) was reacted with succinic anhydride (1.8 g, 1.2 M) in the presence of triethylamine (1.17 mL, 0.56 M). The reaction mixture was incubated for 48 h at 50 °C. Centrifugation was performed at 10,000 rpm (50 mL centrifuge tube, 10,304 ×*g*) for 10 min to discard DMF, and the solid product was washed with DI water (Yield > 90 %). In the final step, an equivalent ratio of EDC (12 mM), NHS (12 mM), and (3.5, 4.2, 5.6, and 19.6 μM) anti-EpCAM was added in a total of 1 mL media containing 8 mg cellulosic materials in phosphate buffered media with pH maintained at 5.5. Quantification of conjugated anti-EpCAM was measured via Bradford assay (Hazra et al., 2020) (Supporting information, Fig. S2, and Table S2).

2.5. *X-ray photoelectron spectroscopy (XPS) and X-ray diffraction analysis (XRD)*

Elemental analysis was performed to confirm the functionalization. X-ray photoelectron spectroscopy (XPS) (Thermo Electron K-Alpha X-ray Photoelectron Spectrometer System) was used to detect the binding energy based on the modification form of the elements. Powder samples were placed on a copper well plate, and pressure was reduced to 1×10^{-7} mTorr. The low-pressure condition was maintained for 24 h before the measurement. The X-ray spot size was 200 μm, and the flood gun was switched on during the measurement to neutralize the surface charge of the samples. Survey scans were performed at a pass energy of 200 eV, 10 scans, dwell time of 10 ms, and energy step size of 1 eV. High-resolution scans were performed for N and Ag at pass energy of 50 eV, 10 scans, dwell time 50 ms, and energy step size of 0.1 eV. Further, we investigated the N/C ratio of CNFs with elemental analysis after the conversion of hydroxyl groups to amines. Elemental analysis was conducted in Atlantic Microlab using combustion techniques with a minimum of 5 mg of vacuum-dried samples. Further X-Ray diffraction analysis (XRD) was carried out on dried sample pallet using Rigaku Ultima IV Versatile X-ray diffractometer with Kα radiation at 40 kV and 40 mA were recorded in the range of 2θ at 5–90°.

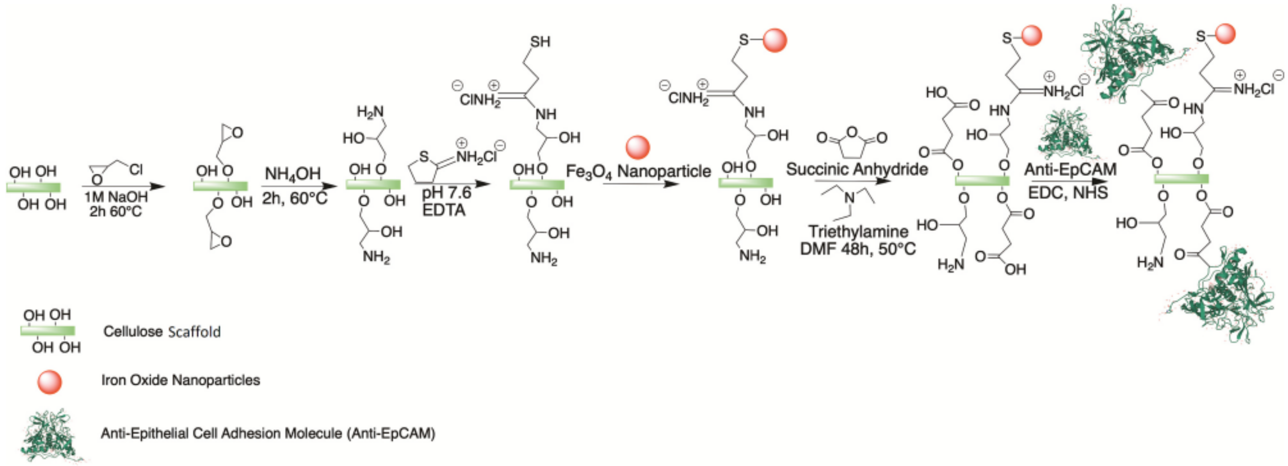

Fig. 2. Synthetic route for generating amine and thiol functional groups on CNC or CNF scaffolds. Fe_3O_4 NPs were conjugated to these cellulosic scaffolds via thiol linkages. Additional hydroxyl groups of CNC or CNF products were partially converted to the carboxylic acid group via succinylation reaction and were conjugated to the anti-EpCAM using EDC/NHS coupling.

2.6. Fourier Transform Infrared Spectrometer (FTIR)

The FTIR experiment was conducted in attenuated total reflection (ATR) mode using a Thermo Scientific Nicolet 8700 system to investigate the functional groups in CNC and CNF scaffolds. The samples were scanned between 4000 and 500 cm^{-1} for 32 repetitive scans (5 statistical replicates). All samples were freeze-dried prior to the ATR-FTIR study.

2.7. Transmission electron microscopy (TEM)

For evaluating the fine structures of nanoparticle-loaded cellulose network structure, transmission electron microscopy (TEM) was performed. A drop of the diluted pristine (unmodified) and Fe_3O_4 NPs-conjugated CNCs/CNFs samples were placed on a 300-mesh formvar-carbon coated copper grid (Ted Pella Inc., Redding, California, USA) for 2 min. The excess liquid on the grid was absorbed using filter paper. The sample was stained using phosphotungstic acid (0.1 %, pH 7–8) for 2 min. Images were collected using a JEOL JEM-1400 Flash transmission electron microscope (JEOL USA) running at 120 kV (JEOL USA, Peabody, Massachusetts, USA) at NDSU Electron Microscopy Core facility (Fargo, North Dakota, USA).

2.8. Dynamic light scattering (DLS) and zeta potential measurement

Dynamic light scattering (DLS) measurements of network structures were carried out in Malvern Zetasizer Nano-ZS90. Sample solutions at a concentration of 1 mg/mL were sonicated in DI water for 10 min in a bath sonicator before the DLS measurement (3 sample replicates, 5 measurements with 5 run/replicates). Before the measurement, all samples were filtered through a syringe filter (Whatman® ReZist® PTFE membrane-based syringe filter with a pore size of 1 μm). Zeta potential was also investigated to analyze the surface charge distribution that governed the electrostatic stability of the colloidal suspensions of network structures using a similar experimental design.

2.9. Magnetic measurement

Magnetic properties of Fe_3O_4 NP-immobilized CNC and CNF scaffolds were measured using a Lakeshore model 7300 Vibrating Sample Magnetometer (VSM) at ambient temperature and at 311 K.

2.10. Cell culture studies

HCT116 cells were procured from NCCS, Pune, India, and were cultured in McCoy media (HiMedia), supplemented with 10 % fetal bovine serum (Invitrogen) and 1 % antibiotic (Penicillin 100 μg/mL, streptomycin 100 μg/mL, Sigma).

2.11. Microscopic evaluation of HCT116 cell capture efficiency of network structures

The artificial cell suspension was prepared by spiking 30 human colon cancer cell line (HCT116) cells in PBS. The resulting HCT 116 cell suspension (1.5 mL) was treated ~500 μg of CNC/CNF products for 15 min. Captured HCT116 cells were entrapped within the cellulose scaffolds and were isolated from the bulk sample under a strong neodymium magnet, N52 graded magnet. The pellet was washed with PBS three times, and after the removal of the magnetic field, the suspension was added to the wells of a 96-well plate. Captured HCT116 cells were fixed with 100 % methanol (chilled at −20 °C) at room temperature for 5 min. Cells were washed in PBS three times for 5 min and incubated with 1 % BSA, 22.5 mg/mL glycine in PBST (PBS + 0.1 % Tween 20) for 30 min to block the unspecific binding of the antibodies. The captured cells were then fixed and immunostained with CK-18 antibody and nuclear-staining probe, DAPI. The cells were imaged and counted using a Zeiss fluorescence microscope (Observer Z1).

2.12. CTC captures efficiency analysis by using head and neck cancer patients' blood samples

Head and neck cancer patient blood samples were treated with red blood cell lysis buffer for 10 min and then centrifuged at 2000 rpm for 15 min. The volume of blood used for CTC isolation is 1.5 mL. The supernatant was discarded, and ~500 μg of CNC/CNF scaffolds were added and incubated with the cell suspension for 15 min. Cell pellets of captured CTCs were separated under 10 min of the magnetic field created by a N52 graded magnet, strong neodymium magnet (25 × 25 × 25 mm^3 dimension and 52 Mega Gauss-Oersteds strength). The captured CTCs were then fixed and immune-stained with CK-18, CD 45, and nuclear-staining probe DAPI. Captured CTCs were scanned using motorized Zeiss fluorescence microscopy, and images were acquired.

3. Results and discussion

3.1. Synthesis of anti-EpCAM-conjugated CNF/CNC scaffolds loaded with magnetic nanoparticles

We adopted a synthetic route reported earlier to prepare magnetically-activable, anti-EpCAM-conjugated CNC/CNF scaffolds (Chen et al., 2021; Hazra et al., 2020; Myung et al., 2012; Singh et al., 2021; Zhang & King, 2017) (Fig. 2). First, hydroxyl groups of CNCs/CNFs were converted to thiols via a two-step reaction process. In the first step, CNCs/CNFs were reacted with epichlorohydrin for 2 h at an elevated temperature (60 °C) under alkaline conditions, followed by ammonium hydroxide treatment. The cellulose-epoxide reaction is stoichiometry and pH-dependent (Dong & Roman, 2007; Li, Shang, et al., 2019; Mahmoud et al., 2010; Porath & Fornstedt, 1970; Zhang et al., 2012). At a higher epichlorohydrin/cellulose ratio, the reaction of epoxides is successful with cellulose, although at a reduced degree of functionalization. Dong et al. reported a condition, where such conversion is maximized by manipulating pH (Dong & Roman, 2007). In case of CNCs, further reactions of sulfates, bisulfate or organosulfates with epoxides require acid catalysis (Aoki et al., 2020). As such, we do not expect a significant influence of sulfates on the reaction that immobilized the epoxide ring on cellulose. As Dong et al., Mahmoud et al. and Zhang et al. proposed, this reaction step converted hydroxyl groups of CNCs/CNFs to amine (Dong & Roman, 2007; Hazra et al., 2020; Mahmoud et al., 2010; Zhang et al., 2012). In the following step, these primary amine functionalized CNFs were reacted with 2-iminothiolane (Trout's salt) at pH 7.6 in the presence of EDTA. Iminothiolane-mediated functionalization of polyamines is a well-established strategy to generate thiol (-SH) functional groups on amine-rich macromolecules (Calderón et al., 2010; Calderón et al., 2011; Hussain et al., 2013). The presence of thiol groups on CNFs was further confirmed using elemental analysis (described later). At the end of these two-step reaction processes, the thiolated CNFs were incubated with Fe_3O_4 NPs. Metal-thiol interactions resulted in the formation of Fe_3O_4 NP-conjugated CNF scaffolds. These scaffolds, after purification, were treated with succinic anhydride. Succinylation produced carboxylic acid (-COOH) randomly along the CNF backbone, assembled to conjugate with the N-terminal of the anti-EpCAM via EDC/NHS coupling. The amount of antibody immobilized was evaluated using the Bradford assay. An extensive purification method consisting of centrifugation has been adopted to generate the purified target product, i.e., anti-EpCAM-conjugated CNFs connected with Fe_3O_4 NPs. Following a similar synthetic route, anti-EpCAM-conjugated CNCs loaded with Fe_3O_4 NPs have also been prepared for head-to-head comparison with CNF-variants for evaluating CTC capture efficiency.

3.2. Elemental, X-ray photoelectron spectroscopy (XPS) and FTIR analysis for network structure characterization

First, elemental analysis was performed to confirm the conversion of cellulosic hydroxyl groups of CNFs to amines by measuring the N and C percentage (Supporting information, Table S3). The analysis showed an increment of N percentage due to amine functionalization of the CNF-hydroxyl groups with epichlorohydrin/NH_4OH treatment (Hazra et al., 2020). For further confirmation, XPS analysis was conducted to identify the presence of nitrogen in these modified cellulose products. The XPS analysis found that the amine-modified CNFs/CNCs showed a prominent peak for N1s compared to pristine CNFs/CNCs. As shown in Fig. 3A, this sharp peak was found at a binding energy of ~399.5 eV, indicating the presence of primary amines present within the modified CNF/CNC scaffolds. Our previous studies also showed the presence of N1s peak at 399 eV when amine functionalized CNCs were synthesized following a similar treatment (Hazra et al., 2020; Lin & Dufresne, 2013; Noel et al., 2011). Two distinct peaks at 163.42 and 169.19 eV binding energy with a 1:4 and 1:3 intensity ratio were also observed in XPS spectra for thiol-modified CNFs/CNCs, which confirmed the presence of S2p of sulfur within the macromolecular scaffold (Castner et al., 1996; Prathapan et al., 2016) (Fig. 3B). The intensity ratio represented that disulfide interactions were less prominent, which renders the remaining thiol groups available for conjugation with Fe_3O_4 NPs. For nanoparticle-conjugated CNFs, Peaks corresponding to the binding energy of ~711 and ~724 eV observed in the XPS spectra can be attributed to the presence of Fe 2P3/2 and Fe 2P1/2 which further confirmed the immobilization of Fe_3O_4 NPs within the modified CNF/CNC scaffolds (Descostes et al., 2000; Omran et al., 2015) (Fig. 3C). A similar result was found in our previous work, where we confirmed the presence of two distinct peaks at 164 and 169 eV for S2p, and 711 and 724 eV for Fe 2p3/2 and Fe 2p1/2, respectively, for thiol and Fe_3O_4 NPs-modified CNCs, demonstrating the successful modification of the CNC network structures via this chemical pathways (Hazra et al., 2020).

FTIR also characterized samples of CNFs/CNCs at different functionalization stages. Spectra corresponding to modified CNF are presented in Fig. 4A, which shows a broad spectral band from 3000 to 3700 cm^{-1} when hydroxyl groups of CNFs were converted to amines. This is due to the overlap of O—H and N—H (primary amine) stretching, indicating the presence of both functional groups because of epichlorohydrin/NH_4OH treatment of native CNFs. With the functionalization of CNFs with primary amines, a distinct band from 1570 to 1630 cm^{-1} was found, which most likely is attributed to the bending vibrations of the N—H groups of primary amines (Ottenhall et al., 2018). Following the iminothiolane reaction and subsequent Fe_3O_4 NP conjugation, FTIR was conducted on the purified product. A weak band at 2550–2572 cm^{-1} was observed in the product, which can be attributed to the S—H stretching (Kim et al., 2005). Succinylation of Fe_3O_4-conjugated CNFs partially converted hydroxyl groups to carboxylic groups. Two clear bands at 1725 and 1658 cm^{-1} were observed in the succinylated, Fe_3O_4-conjugated cellulosic products, which could be attributed to the C═O and C—H stretching of the carboxylic acid moieties (Gipson et al., 2015; Montanari et al., 2021). With modified CNCs, a similar pattern of FTIR bands was observed, which is presented in Fig. 4B.

Further XRD analysis demonstrated the crystallinity nature of CNCs/CNFs in pristine and post-functionalization conditions (Supporting

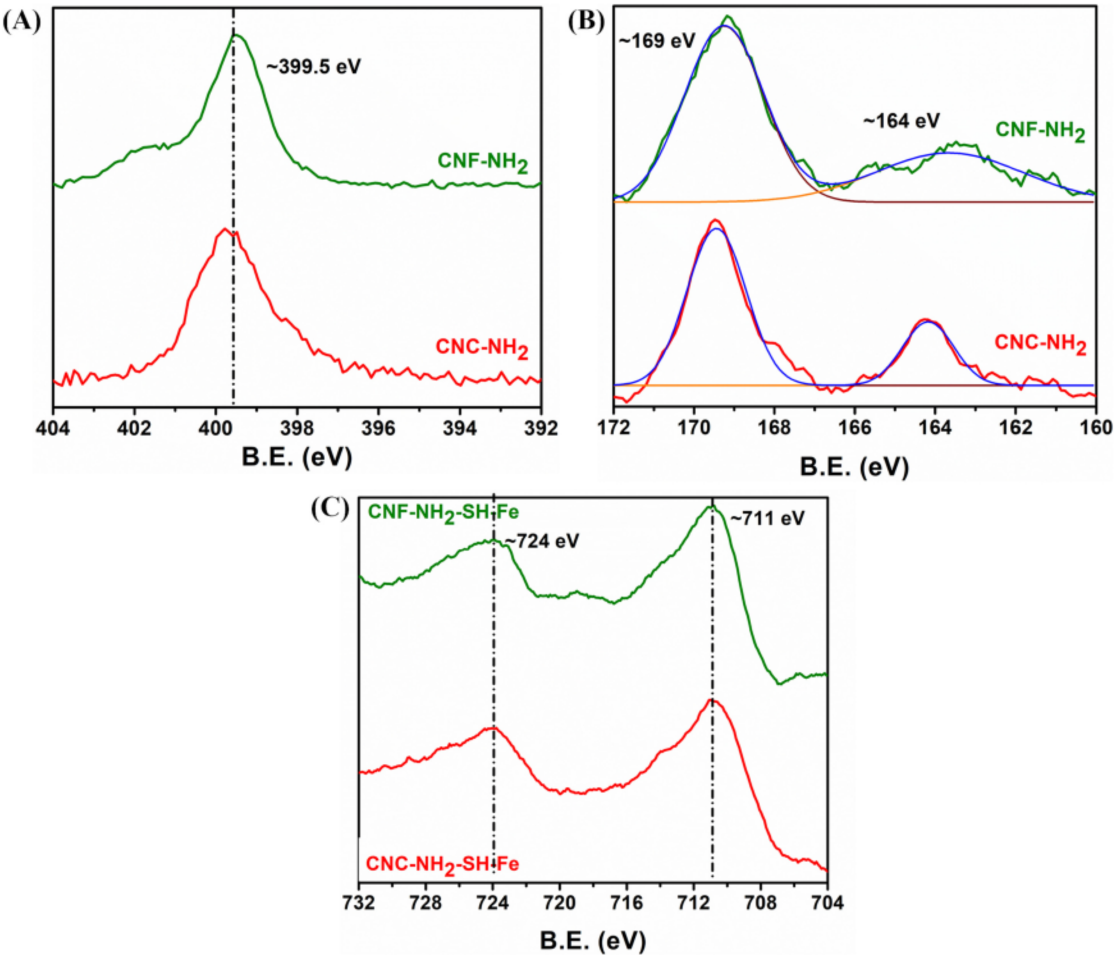

Fig. 3. Identification of modified CNF samples using (A) XPS spectra to confirm primary amine groups at ~399.5 eV. (B) Conjugated thiol (-SH) groups after iminothiolane reaction, and (C) Fe_3O_4 NP conjugation where peaks for Fe 2P3/2 and Fe 2P1/2 were identifiable. Gaussian fitting of the peaks was used to identify the peaks corresponding to different species.

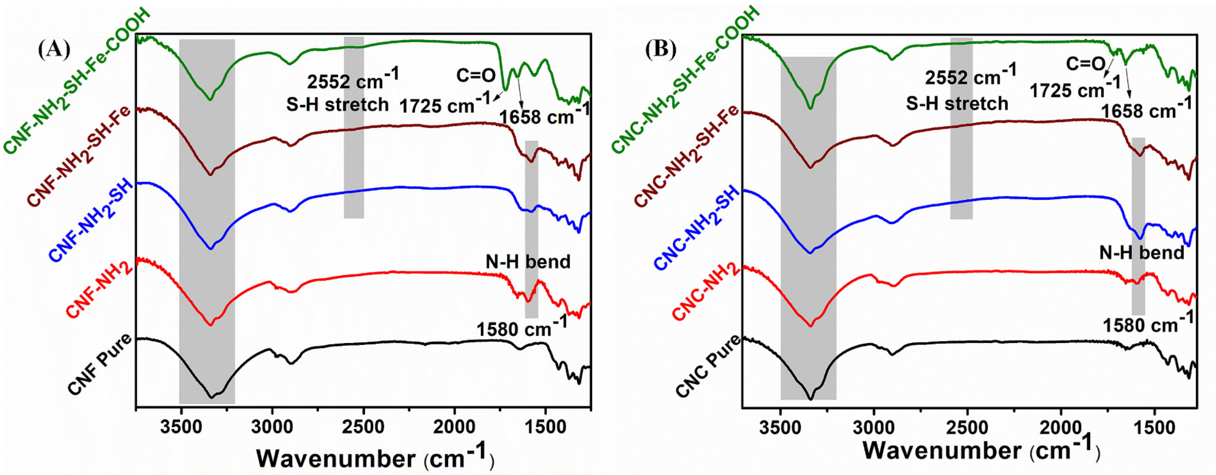

Fig. 4. FTIR spectra of pure and modified (A) CNFs and (B) CNCs after the reaction of the cellulosic materials with amines (via epichlorohydrin/NH_4OH), thiols (via reaction with Traut's reagent), Fe_3O_4 NPs, and with succinic anhydride.

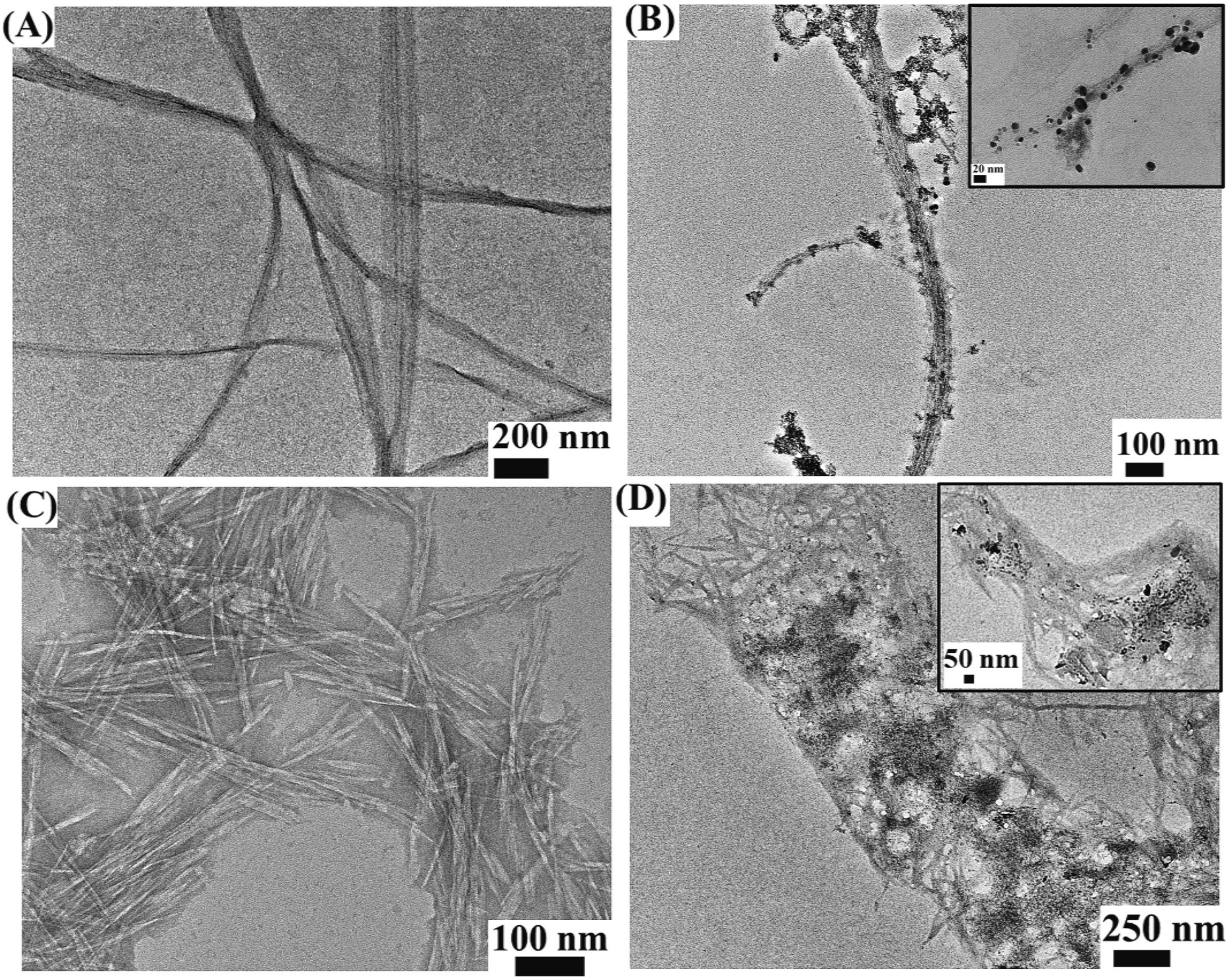

Fig. 5. TEM micrograph of (A) pristine (unmodified) CNFs and (B) Fe_3O_4 NPs decorated CNFs; TEM micrograph of (C) pristine (unmodified) CNCs and (D) Fe_3O_4 NPs decorated CNCs. Both CNCs and CNFs were found to form interaction between the nanoparticles through secondary interactions operating within the crystalline and fibrous domain of these cellulosic products.

information, Fig. S3). Pristine CNCs and CNFs experienced a reduction in peak intensity after functionalization, which was reduced due to the conversion of functional groups and a decrease in crystallinity. This result further supported the successful functionalization.

3.3. Particle size, surface charge, and microstructural features of Fe_3O_4 NPs-conjugated CNFs in aqueous solution

Microstructures of pristine and Fe_3O_4 NP-conjugated CNFs were analyzed by TEM. As shown in Fig. 5A, pristine CNFs with each string are composed of bundles of nanofibers at micrometer length. Modifying CNFs with thiol groups and subsequent Fe_3O_4 NP-conjugation resulted in the immobilization of Fe_3O_4 NPs along the surface of nanofiber bundles (Figs. 5B and S4). Electron microscopy further revealed that Fe_3O_4 NP was found to be ~15 ± 6 nm in diameter when stabilized within the network structure of thiol-modified CNFs. We have previously reported nanoscale structures of Fe_3O_4 NPs conjugated within the CNC scaffold, which we further validated in this study for comparison purpose (Hazra et al., 2020). Fig. 5C shows the pristine CNCs that are 129 ± 4 nm long and 8 ± 2 nm wide. These crystals were found to form an interaction among them. Post-functionalization with thiol groups resulted in the attachment of the Fe_3O_4 NPs along the surface of the CNC scaffolds (Fig. 5D). The interaction between cellulosic scaffold was most likely formed due to secondary interactions within the crystalline and fibrous domains of CNC and CNFs, respectively. It has been previously reported that pristine cellulose, whether nanofibers or nanocrystals, can form an interaction between the fibers or crystals (Balakrishnan et al., 2018; Xu et al., 2013). Cellulose has unique interaction properties, such as secondary interactions between the cellulose fibers or crystals. High aspect ratios and large surface areas of cellulose nanofibers and nanocrystals enable a high number of interaction sites.

The hydrodynamic diameter (D_H) of pristine (unmodified) CNCs or CNFs and their Fe_3O_4 NP-conjugated variants were investigated using dynamic light scattering (DLS) measurements. For these experiments, 1 mg/mL of CNCs or CNFs were dispersed in water, and the aqueous dispersion was filtered through a syringe filter (Whatman® ReZist® PTFE membrane-based syringe filter with a pore size of 1 μm) (Fig. 6A). It was found that pristine or unmodified CNCs showed a hydrodynamic diameter of 120 ± 14 nm. Interestingly for CNF aggregates, particles with D_H of 160 ± 30 nm and 670 ± 35 nm were observed. While the D_H of Fe_3O_4 NPs-loaded CNC scaffolds was 240 ± 15 nm, nanoparticle-loaded CNF scaffolds (Fig. 6A) demonstrated an average diameter of 530 ± 27 nm. To investigate the origin and compare the aqueous colloidal stability of Fe_3O_4 NP-loaded CNC and CNF nano scaffolds, zeta (ζ-) potential was measured. Fig. 6B shows the evolution of the ζ- potential after different stages of functionalization of CNC and CNF nano scaffolds. We observed that, while ζ- potential of the unmodified CNCs were −22 mV, unmodified CNFs showed a ζ-potential of −23 mV. Following the amination reaction of CNCs and CNFs, reaction products showed reduced ζ- potential of −8 mV and −10 mV, respectively. Amination reaction generates primary amine ($-NH_2$) groups on the surface. These groups increase the positive charge density on the surface of the nanomaterial. The degree of amination (number of amino or ammonium groups per unit of cellulose) increases the cationic charge density and reduces the anionic charge density of the surface. Since the amination reaction is partial, therefore, both CNF and CNC suspensions still show negative surface charge, but the magnitude is reduced. Thiol conjugation to amine groups of CNCs and CNFs shifted ζ-potential to −18 mV for CNCs and −20 mV for CNF thiols. When thiol groups are functionalized onto the surface of the aminated cellulose (less negative zeta potential product), amino groups are converted to thiols, further recovering the negative surface potential. Finally, the addition of Fe_3O_4 NPs and their attachment to CNCs or CNFs through these thiol groups increased the zeta potential to reach −31 mV and −32 mV, respectively. While ζ-potential is a critical parameter to control the stability of nanostructures in solution, such stability is mostly contributed by ionic/electrostatic repulsion between the colloidal aggregates. Combined DLS and ζ-potential studies showed that CNFs showed larger diameter aggregates (at least 2-fold) than those of CNC-based systems, and the surface charges for both species are mostly similar (−31 to −32 mV).

To identify the origin of ζ-potential for CNFs and CNCs, surface charge densities of cellulose scaffolds were evaluated (Supporting information, Fig. S5, and Table S4). CNF and CNC-based scaffolds showed a similar pattern of surface charge increment after the conversion of hydroxyl to the amine. Hydroxyl (-OH) surface charge density is naturally low, as -OH is not highly charged. The amination process conjugated amine groups in the CNC/CNF scaffold and elevated the surface charge density. This happened as $-NH_2$ groups were basic and released protons due to ionization, resulting in a positively charged surface. Further functionalization increased surface charge density after the reaction between Traut's reagent (2-iminothiolane) and primary amines. Although thiol is a negatively charged group close to neutral in charge density, Traut's reagent reaction with primary amine generated an additional charge density onto the scaffold. The addition of thiol groups

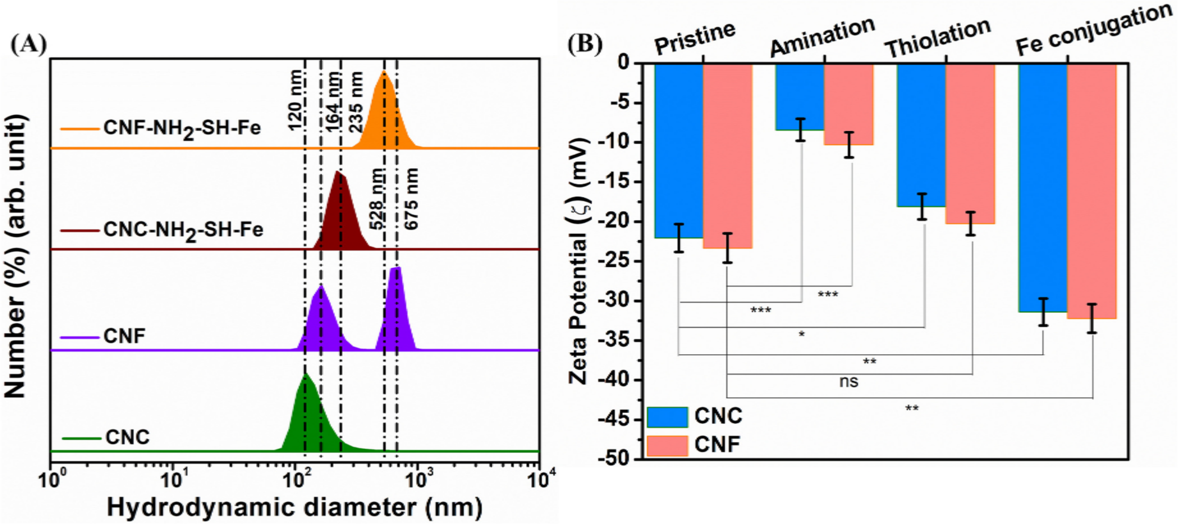

Fig. 6. Nanoscale features of CNC and CNF scaffolds. (A) Hydrodynamic diameter for unmodified CNCs and CNFs, Fe_3O_4 NP-conjugated CNCs and CNFs, and (B) Surface charge (ζ-) potential of unmodified CNCs and CNFs, Fe_3O_4 NP-conjugated CNCs and CNFs ($n = 3$; Standard deviation based on (n-1); statistical analysis based on two-sample assuming unequal variances t-test, ns for $P > 0.05$, * for $P < 0.05$, ** for $P < 0.01$ and *** for $P < 0.001$).

promoted the protonation of nearby amine groups, which increased overall surface charge density. Followed by Traut's reaction (thiol addition), Fe_3O_4 NP conjugation showed a further increment of surface charge density (thiol donated electrons to Fe_3O_4 NPs). During the complexation of thiol (-SH) and Fe_3O_4 NP, negatively charged thiol groups introduced negative charges to the complex, resulting in an elevation of surface charge density. This result demonstrated that Fe_3O_4 NP-conjugated CNC/CNF scaffolds were very stable and less likely to aggregate due to repulsive force between charged scaffolds. Charged groups repelled each other and expanded over a large area by increasing surface charge density.

3.4. Magnetic property measurement on Fe_3O_4 NP-immobilized CNC and CNF scaffolds

Using high-resolution transmission electron microscopy (HRTEM) crystal plane analysis, earlier, we reported that the Fe_3O_4 NPs, when synthesized within the CNC scaffolds, were magnetite in nature with a d-spacing of 2.9 Å (Hazra et al., 2020). Previously explored nanoparticle-loaded cellulosic scaffolds can be separated using the application of a magnetic field (Hazra et al., 2020). In this current study, we quantified the magnetic properties of CNF scaffolds loaded with Fe_3O_4 NPs and compared the properties of these nanostructures with that obtained from CNCs loaded with Fe_3O_4 NPs. The objective of this experiment was to evaluate how the presence of magnetic nanoparticles influences interactions of CNFs or CNC scaffolds with a field of given magnetic strength. We observed that a magnetic field created by a permanent magnet (neodymium magnet, N52 graded magnet) kept adjacent to the wall of the container loaded with CNF, or CNC scaffolds caused the movement of the scaffolds towards the direction of the field, leading to the formation of a thin aggregation film on the surface of the container closer to the magnet. Scaffold particles were separated from the solution even with a moderately intense magnetic field application. Due to their size and structure, the magnetic nanocrystals were expected to exhibit super-paramagnetic behavior at moderate field and frequency (0–150 Oe, 0–1000 kHz) range (Atluri et al., 2018; Fortin et al., 2007). Fe_3O_4 NP-loaded CNCs and CNFs' magnetic behavior was probed at room temperature and 311 K (Fig. 7A–B). Minimal to no hysteresis response was observed, indicating these systems' super-paramagnetic behavior. The magnetic loop of these hysteresis curves was also symmetric about the center for both temperatures. Slight agitation brought the cellulosic scaffolds back into the solution once the magnetic field was removed. Such gentle separation of cellulose scaffolds using a magnetic field is practically significant, as magnetic separation will provide ease of separation of CTCs without exposing the cells to harsh reagents or agitation during the analytical procedure.

3.5. Cell capture efficiency of CNF and CNC network structures

We compared the CTC capture efficiency of Fe_3O_4 NPs-loaded and anti-EpCAM-conjugated CNF and CNC scaffolds against HCT116 cells. Fig. 8 shows the representative images of cells post-capture. Cells were co-stained with DAPI and eosin. DAPI was used as a nuclear staining dye, and eosin was used to stain cell cytoplasm to confirm captured cells (Biglione et al., 2018).

A quantitative analysis of such capture efficiency is shown in Table 1. For this experiment, we used HCT116 cells that express antigens for the anti-EpCAM. It was observed that CTC capture efficiency for CNC and CNF-based scaffolds increased with increasing the content of anti-EpCAM-conjugated on the scaffold surface. For example, the maximum cell capture efficiency (~93,33 %) was observed for CNC scaffolds, where 23 μg anti-EpCAM was conjugated per mg of cellulosic materials. On the other hand, for CNF network structures, the highest capture efficiency (66.66 %) was observed when 55 μg anti-EpCAM was conjugated per mg of cellulose content. Surprisingly, even at a reduced level of antibody content, i.e., ~14 μg anti-EpCAM conjugated per mg of cellulosic materials, CNC scaffolds retained 70 % cell capturing efficiency. (Sample 1A to Sample 1C in Table 1). While we have increased >2 fold of Fe_3O_4 NP with respect to Anti-EpCAM from 0.12 to 0.27 (Fe_3O_4 NP: Anti-EpCAM), capture efficiency remained similar (only ~3 % increment) (Sample 1B to 1C, Table 1). This result demonstrated that capture efficiency slightly depends on the concentration of Fe_3O_4 NP but mostly depends on Anti-EpCAM. Despite high antibody content (i.e., 55 μg anti-EpCAM per mg cellulosic content), CNF nanomaterials demonstrated a maximum of ~67 % CTC capturing capacity (Sample 2A in Table 1). Scaffolds composed of similar concentrations of anti-EpCAM and Fe_3O_4 NPs showed similar order of CTC capture efficiency (please note samples 2B and 2C). These results indicate that CNC scaffold is more efficient than CNF in CTC capturing efficiency. However, to clarify this further evaluation is needed using more comparable Fe_3O_4 NP contents between the tested CNF and CNC systems, and this is out of the scope of the present work. We observed that the hydrodynamic diameters of CNC scaffolds were smaller (~250 nm) than those of CNF-based scaffolds (~600 nm). The smaller hydrodynamic diameter of CNC scaffolds most likely promoted efficient interactions and capture of HCT116 cells by their surface receptors compared to those of CNF scaffolds, leading to higher capture efficiency exhibited by CNC variants.

3.6. CTC capture efficiency analysis by using head and neck cancer patient blood samples

Compared to a clinically validated platform, i.e., OncoDiscover®, used for CTC detection, both CNC and CNF scaffolds showed significant CTC capturing potential. OncoDisover® platform comprises multifunctional, magneto-polymeric materials bearing anti-EpCAM that interact

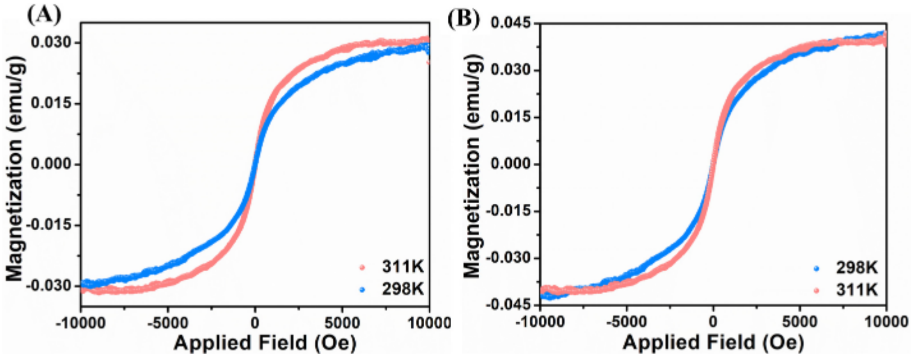

Fig. 7. Applied field vs. magnetization plot for (A) Fe_3O_4 NP-immobilized CNC and (B) Fe_3O_4 NP immobilized CNF scaffolds at ambient temperature and at 311 K, demonstrating minimal hysteresis response for the designed systems.

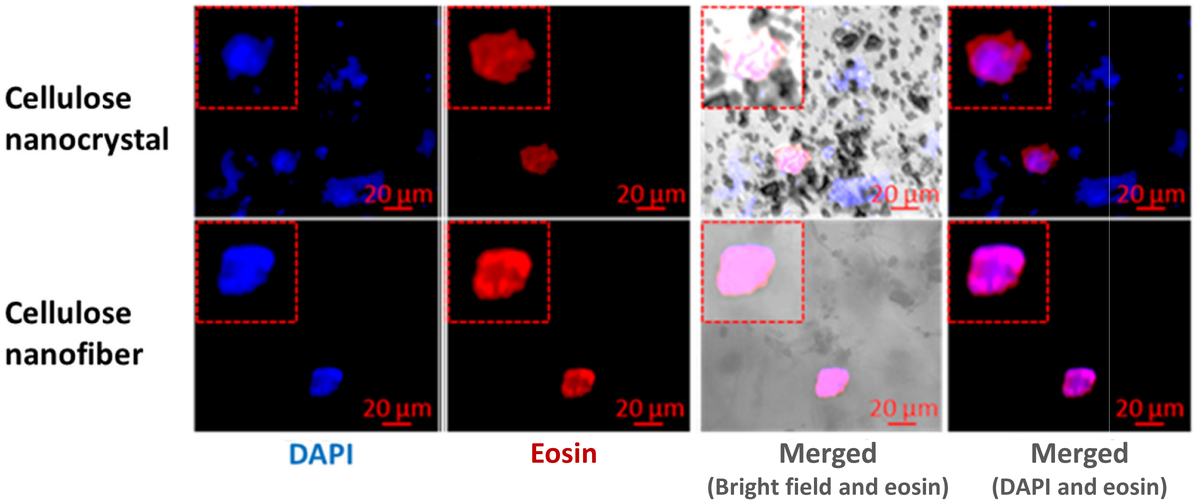

Fig. 8. Representative images of HCT 116 cells captured using Fe_3O_4 NPs and anti-EpCAM-conjugated scaffolds composed of CNC (top panel) and CNF (bottom panel). Cells were stained with DAPI and Eosin. Merged image shows overlay images of cells stained with either DAPI, Eosin and bright filed channel.

Table 1
Sample formulations investigated for the evaluation of cell capture efficiency.

Sample	Anti-EpCAM content[a]	Iron oxide content[b]	Cells captured (30 cells added)			Average cells captured	Average cell capture efficiency (%)
			n1	n2	n3		
1A- CNC-$Fe_3O_4^{(+SH,\ +EpCAM)}$	23	1.25	27	28	29	28 ± 1	93.33 ± 3.33
1B- CNC-$Fe_3O_4^{(+SH,\ +EpCAM)}$	15	1.87	20	22	19	20.3 ± 1.53	67.77 ± 5.09
1C- CNC-$Fe_3O_4^{(+SH,\ +EpCAM)}$	14	3.75	22	22	19	21 ± 1.73	70.00 ± 5.77
1D- CNC-$Fe_3O_4^{(-SH,\ -EpCAM)}$	00	5.25	00	00	00	00	00
2A- CNF-$Fe_3O_4^{(+SH,\ +EpCAM)}$	55	1.00	19	20	21	20 ± 1	66.66 ± 3.33
2B- CNF-$Fe_3O_4^{(+SH,\ +EpCAM)}$	15	0.75	18	19	16	17.7 ± 1.53	58.88 ± 5.09
2C- CNF-$Fe_3O_4^{(+SH,\ +EpCAM)}$	10	0.50	15	18	17	16.7 ± 1.53	55.55 ± 5.09
2D- CNF-$Fe_3O_4^{(-SH,\ -EpCAM)}$	00	4.75	00	00	00	00	00

[a] The content of Anti-EpCAM in scaffolds was measured (Supporting information, Fig. S2, and Table S2) via Bradford assay with an absorbance maximum at 595 nm. The amount was tabulated in μg of Anti-EpCAM per mg of CNC/CNF.

[b] The iron content of different scaffolds was measured via UV–Vis spectroscopic analysis at an absorption maxima of 370 nm (Hazra et al., 2020). The amount was tabulated in mg Fe_3O_4 NP per mg of CNC/CNF (Supporting information, Table S2); Standard deviation evaluated based on (n-1); Statistical analysis: Supporting information, Fig. S6 and Table S5.

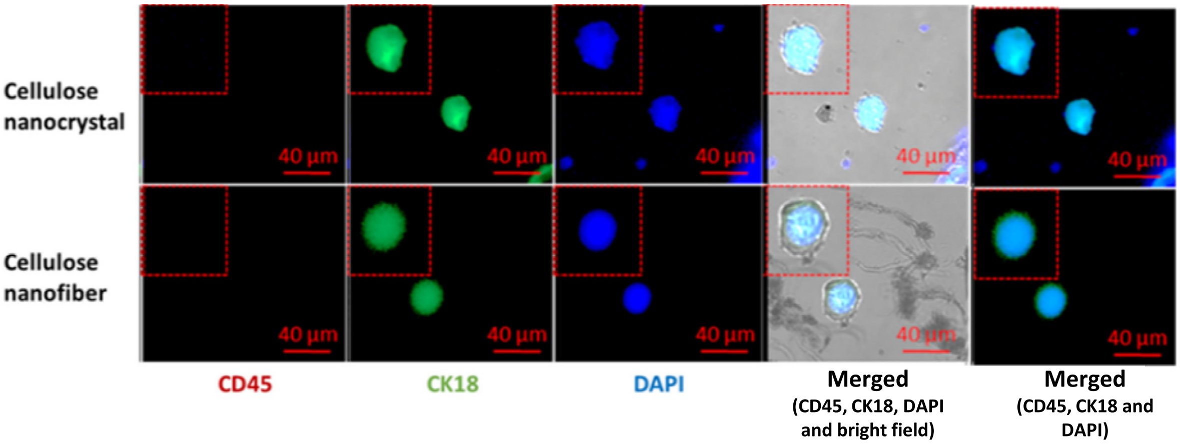

Fig. 9. Representative fluorescence images of circulating tumor cells (CTCs) isolated by Fe_3O_4 NPs and anti-EpCAM-conjugated CNC/CNF scaffolds from blood samples of head and neck cancer patients ($n = 6$). CK18 and CD45 markers are shown in green and red channels, respectively. Nuclei are stained with DAPI (blue), and multichannel composites are merged. Merged image is overlay image of either DAPI, anti-CK18 Ab, anti-CD45 Ab and bright filed channels.

with CTCs (Khandare et al., 2016). Detection of CTCs either via CNC-, CNF- or OncoDiscover® platforms was carried out from 1.5 mL of HNC patients' blood samples. The capture efficiency of CTCs for these platforms was evaluated by fluorescence microscopy. Fig. 9 shows the fluorescence imaging of CTCs isolated from cancer patients' blood samples by CNC or CNF scaffolds, where CK18 and CD 45 were used as clinically validated biomarkers for CTCs. In Fig. 9, antibodies recognizing CK18 and CD45 are shown in green and red channels, respectively. Cell nuclei were stained with DAPI (blue), and multichannel composite images are also illustrated. When analyzed by fluorescence microscopy, fibrous materials were observed along with cancer cells for CNC and CNF scaffolds (Fig. 9, merged), most likely indicating the interacting network structures with cell membranes. Further study is undergoing in our laboratories to confirm these membrane-bound structures. We also tested the viability of the scaffold-captured cells with CNF scaffolds. Cell viability was tested using Alamar Blue assay (Supporting information, Fig. S7). The results demonstrated that cells were viable after capture and isolation with the magnetic field.

Quantitatively, CNC scaffolds containing 23, 15, and 14 μg anti-EpCAM per mg of cellulosic materials showed almost similar CTC capturing ability as that of the commercially available OncoDiscover® platform (Table 2). The difference in total CTC capture ratio of OncoDiscover® to CNC scaffolds was found to be 50, 100, and 67 % (for 2:1, 2:2, and 3:2 capture ratio of OncoDiscover®: CNC system). This defines that the CNC-based system showed an overall ~72 % capture efficiency (for a 7:5 capture ratio of OncoDiscover®: CNC system) irrespective of the antibody content. However, this difference is less significant, considering the blood samples of cancer patients are highly heterogeneous for the presence and distribution of CTCs. Whereas the difference in total CTC capture ratio of OncoDiscover® to CNF scaffolds was found to be 50 and 33 % (for 2:1,0:0, and 3:1 capture ratio of OncoDiscover®: CNF system). This defines that the CNF-based system showed an overall ~40 % capture efficiency (for a 5:2 capture ratio of OncoDiscover®: CNC system) irrespective of the antibody content. This could be attributed to the structural flexibility and very high aspect ratio of CNFs that prevented facile interactions of CTCs with the CNF-based scaffold. Of note that the OncoDiscover® platform, which has been clinically validated and approved by the regulatory body (Drug Controller General of India, DCGI, and on Indian phenotypes) when tested on large clinical sample size ($n = 1000$) from patients' blood samples in various solid cancers, such as head and neck, lung, breast, and colorectal cancer. CNC-based systems showed ~28 % lower capture efficiency than commercially available OncoDiscover® systems. The main drawback of commercially available OncoDiscover® systems is using a toxic dendrimer system to capture CTCs, whereas we have used biocompatible, nontoxic materials for CTC capturing. The CNC scaffolds tested in this study indicated a CTC capturing ability in a limited number of cancer patient blood samples, thus warranting further studies for the potential use of the scaffold in clinical settings.

4. Discussion

The rarity and heterogeneity of CTCs in patient blood samples render efficient isolation, enumeration, and comprehensive characterization of these cells extremely challenging. These challenges include tumor evolution, staging, biomarker expression, epithelial-to-mesenchymal, and mesenchymal-to-epithelial transition (EMT/MET) phenomena, and distributional heterogeneity even for the same cancer patient, further complicate the reliability of CTC enumeration as a measure for clinical diagnosis, prognosis and clinical decision making (Alix-Panabières & Pantel, 2014). To address such unmet challenges, designing and utilizing a novel and efficient CTC capture and enumeration platform and validated CTC enrichment approaches become the crucial need of the hour. Herein, two novels, magnetically separable CTC isolation scaffolds, i.e., anti-EpCAM-conjugated cellulose nanofibers (CNFs) and cellulose nanocrystals (CNCs), have been developed and tested for capturing CTC-mimicking (HCT116 cell lines) in vitro, and primary CTCs from HNC patients' blood samples. In both cases, the CNC scaffolds indicated similar efficiency and sensitivity towards capturing EpCAM$^+$ CTCs compared to their CNF-based analogues. This is most likely due to the smaller hydrodynamic diameters of CNCs, the primary scaffold-forming materials of the former, that promoted suitable interactions between the cells and the scaffold. Our results differ significantly from the CTC-capturing scaffolds prepared earlier by different groups using synthetic nanofibers. For example, Tseng et al. reported the manufacturing of synthetic nanofibers-based Anti-EpCAM conjugated electrospun mats composed of a mixture of poly(sulfobetaine methacrylate) (PSBMA) and poly(acrylic acid) (PAA) into nylon-6. This system demonstrated ~75, 55.6, and 70 % capturing efficiency for DLD-1, HCT116, and HT-29 colorectal cancer cell lines respectively (Tseng et al., 2016). Similarly, Anti-EpCAM conjugated electrospun mats composed of poly(ethylene oxide) (PEO), and nylon-6 fibers showed 40–70 % capture efficiency for DLD-1, HCT116, and HT-29 colorectal cancer cell lines (Lee et al., 2018). Unlike PSBMA, PAA, PEO, or nylon-based fibers, CNFs show a significantly higher number of sites where probable secondary interactions can take place. These sites are more available in CNFs than those in CNCs. CNFs are long and fibrous, whereas CNCs are short, rigid, and crystal-like particles. This structural variation results in CNFs demonstrating a comparatively higher number of interaction sites (secondary interaction) than CNCs. CNFs have a high aspect ratio, which enhances the chances of intermolecular interactions (Balakrishnan et al., 2018; Xu et al., 2013). Due to these higher number of interaction sites, CNFs tend to exist as bundles of nanofibers within the scaffolds, potentially providing steric hindrance against antibody presentation and engagement with CTCs. In the comparison capturing process, Kumar et al. developed CNF based microfluidic chip functionalized with Anti-EpCAM and captured the HCT116 cell line with 79–98 % efficiency with 5 μL/min for 10 min flow (Kumar et al., 2020). One of the challenges of these microfluidic channels is low capturing efficiency in high flow rate, low contact time with the channel, and low contact point for large volume blood. Our magnetic suspension does not have potential clogging challenges and has whole access to contact with CTCs, even in large-volume blood. To overcome the challenges related to pore-clogging for filter-type CTC capturing scaffolds (Adams et al., 2014; Lee et al., 2019; Zheng et al., 2011), nanoscale CTC-entrapment platforms composed of multivalent dendrimers (such as PAMAM) have been reported (Bu et al., 2020; Meng et al., 2020; Myung et al., 2011; Myung et al., 2015). These PAMAM-derived CTC capturing platforms were conjugated with EpCAM, epidermal growth factor receptor (EGFR), folic acid receptors (FR), carbonic anhydrase IX (CA9), hepatocyte growth factor receptor (c-Met). These systems showed ~80–90 % capture efficiency towards nonsmall cell lung cancer (NSCLC) cells, ovarian cancer cells (SKOV3) cells, ACHN, and 786-O renal cell carcinoma (RCC) cell lines. In comparison, the CNC-based CTC capturing scaffold presented in this study showed ~93 % capture efficiency. Compared to the clinically validated OncoDiscover® platform, CNC scaffolds emerged as promising candidates for further evaluation as clinically relevant CTC isolation platforms. Furthermore, we observed that CNC scaffolds could capture and separate CTCs from other blood components under very mild conditions. This could greatly enhance downstream analyses of captured CTCs

Table 2
Anti-EpCAM content in CNC or CNF scaffolds and comparison of CTC capture efficiency of these scaffolds with that of OncoDiscover® platform from blood samples of head and neck cancer patients ($N = 6$).

Sample	Anti-EpCAM content (μg)[a]	No. of CTCs captured	
		OncoDiscover®	CNC/ CNF
1A- CNC-$\text{Fe}_3\text{O}_4^{(+\text{SH},}{}_{+\text{EpCAM})}$	23	2	1
1B- CNC-$\text{Fe}_3\text{O}_4^{(+\text{SH},}{}_{+\text{EpCAM})}$	15	2	2
1C- CNC-$\text{Fe}_3\text{O}_4^{(+\text{SH},}{}_{+\text{EpCAM})}$	14	3	2
2A- CNF-$\text{Fe}_3\text{O}_4^{(+\text{SH},}{}_{+\text{EpCAM})}$	55	2	1
2B- CNF-$\text{Fe}_3\text{O}_4^{(+\text{SH},}{}_{+\text{EpCAM})}$	15	0	0
2C- CNF-$\text{Fe}_3\text{O}_4^{(+\text{SH},}{}_{+\text{EpCAM})}$	10	3	1

[a] Per mg of cellulosic content.

through comprehensive molecular and single-cell genomic/transcriptomic techniques for characterization, thereby accelerating the identification of actionable therapeutic targets and anti-cancer drug development (Li et al., 2018). The implications of such novel innovations are far-reaching in transforming cancer disease management and precision oncology, which we envision to impact the progression-free/disease-free survival (PFS/DFS) of cancer patients.

5. Conclusions

In this current study, we successfully designed anti-EpCAM-conjugated and Fe_3O_4 NP-immobilized nanocellulose scaffolds to enumerate CTCs. We compared CNCs and CNFs as nanoscale scaffold-forming materials for capturing and isolating CTCs from patients' blood samples. We compared the efficiency of the nanocellulose scaffolds against a clinically validated and commercially available product, OncoDiscover®. Chemical functionalization of the hydroxyl group of CNCs/CNFs was conducted for immobilizing Fe_3O_4 NPs to the scaffolds, thus rendering the scaffolds magnetically active. Finally, anti-EpCAM was conjugated onto the scaffold surfaces to promote scaffold interactions with CTCs overexpressing the EpCAM receptors. We observed that the presentation and distribution of anti-EpCAM on scaffold surfaces, the presence or absence of magnetically active modules within the scaffold network, and the hydrodynamic features of the scaffolds played a pivotal role in determining their CTC capture efficiency. Further, this current study also revealed that scaffold composed of CNCs seems to perform better in capturing CTCs than CNFs. Compared with commercially standard OncoDiscover®, anti-EpCAM-conjugated, Fe_3O_4 NP-immobilized CNC scaffolds showed comparable capture efficiency, warranting further studies for potential use in clinical settings. New CTC capture platforms with commercial accessibility, sustainability, and affordability, are a critical and unmet need for cancer patients' management, especially in low-resource settings.

CRediT authorship contribution statement

Name	Contribution
Raj Shankar Hazra	Experimentation (chemistry/materials), data acquisition and analysis, writing manuscripts.
Narendra Kale	Experimentation (cell biology, microscopy), data analysis, writing manuscripts, graphics and illustrations.
Camden Boyle	Experimentation (magnetic properties), data analysis
Kayla B. Molina	Experimentation (chemistry/materials), data analysis
Alain D' Souza	Experimentation (biology), data analysis
Gourishankar Aland	Experimentation (biology), data analysis
Long Jiang	Senior authors (mechanics of materials), data analysis, manuscript writing and review
Pankaj Chaturvedi	Senior author (clinical), manuscript writing and review
Santaneel Ghosh	Senior author (magnetic properties), data analysis, manuscript writing
Sanku Mallik	Senior author (cell biology, microscopy), data analysis
Jayant Khandare	Corresponding author (cancer biology, correspondence with clinicians, patient sample procurement), data analysis, manuscript writing, editing, review, conception of idea
Mohiuddin Quadir	Corresponding author (chemistry/materials), funding procurement, resource allocation, data analysis, manuscript writing, editing, review, conception of idea.

Declaration of competing interest

The authors declare that they have no known competing financial interests or personal relationships that could have appeared to influence the work reported in this paper.

Data availability

Electronically supplementary information is included and available upon request.

Acknowledgments

The authors would like to thank Scott Payne and Jayma Moore for TEM imaging.

Ethics statement

The Institutional Ethical Committee of TATA Memorial Hospital (IEC/1117/1903/001) approved clinical blood-sampling procedures, and informed consent was obtained for patient participation. These protocols were approved by the Institutional Ethical Committee of TATA Memorial Hospital, and the methods were carried out in accordance with the relevant guidelines and regulations.

General information

The manuscript was written through the contributions of all authors. All authors have given approval for the final version of the manuscript.

Funding

Research presented in this paper was supported by the National Science Foundation under NSF EPSCoR Track-1 Cooperative Agreement OIA #1946202 (MQ). Partial support was received from the NSF Award Number: 2239629 (MQ). NSF grant no. IIA1355466 from the North Dakota Established Program to Stimulate Competitive Research (EPSCoR) through the Center for Sustainable Materials Science (CSMS) is also acknowledged. Any opinions, findings, conclusions, or recommendations expressed are those of the authors and do not necessarily reflect the views of the National Science Foundation. Notes The authors declare no competing financial interest. Further, NIGMS grant 2R01GM114080 is acknowledged (SM), and partial support was also received from NASA-Missouri Space Grant Consortium - Subaward No. 00070245-11 (SG).

Appendix A. Supplementary data

Supplementary data to this article can be found online at https://doi.org/10.1016/j.carbpol.2023.121418.

References

Abdul Khalil, H., Adnan, A., Yahya, E. B., Olaiya, N., Safrida, S., Hossain, M. S., … Oyekanmi, A. (2020). A review on plant cellulose nanofibre-based aerogels for biomedical applications. *Polymers, 12*(8), 1759.

Adams, D. L., Zhu, P., Makarova, O. V., Martin, S. S., Charpentier, M., Chumsri, S., … Tang, C.-M. (2014). The systematic study of circulating tumor cell isolation using lithographic microfilters. *RSC Advances, 4*(9), 4334–4342.

Alix-Panabières, C., & Pantel, K. (2014). Challenges in circulating tumour cell research. *Nature Reviews Cancer, 14*(9), 623–631.

Aoki, E., Sarrimanolis, J. N., Lyon, S. A., & Elrod, M. J. (2020). Determining the relative reactivity of sulfate, bisulfate, and organosulfates with epoxides on secondary organic aerosol. *ACS Earth and Space Chemistry, 4*(10), 1793–1801.

Atluri, R., Atmaramani, R., Tharaka, G., McCallister, T., Peng, J., Diercks, D., GhoshMitra, S., & Ghosh, S. (2018). Photo-magnetic irradiation-mediated multimodal therapy of neuroblastoma cells using a cluster of multifunctional nanostructures. *Nanomaterials, 8*(10).

Balakrishnan, P., Gopi, S., Geethamma, V., Kalarikkal, N., & Thomas, S. (2018). Cellulose nanofiber vs nanocrystals from pineapple leaf fiber: A comparative studies on reinforcing efficiency on starch nanocomposites. In *Macromolecular symposia* (p. 1800102). Wiley Online Library.

Banerjee, S. S., & Chen, D.-H. (2007). Fast removal of copper ions by gum arabic modified magnetic nano-adsorbent. *Journal of Hazardous Materials, 147*(3), 792–799.

Biglione, C., Bergueiro, J., Asadian-Birjand, M., Weise, C., Khobragade, V., Chate, G., … Calderón, M. (2018). Optimizing circulating tumor cells' capture efficiency of magnetic nanogels by transferrin decoration. *Polymers, 10*(2), 174.

Boya, M., Ozkaya-Ahmadov, T., Swain, B. E., Chu, C.-H., Asmare, N., Civelekoglu, O., … Sarioglu, A. F. (2022). High throughput, label-free isolation of circulating tumor cell clusters in meshed microwells. *Nature Communications, 13*(1), 3385.

Bu, J., Nair, A., Kubiatowicz, L. J., Poellmann, M. J., Jeong, W.-j., Reyes-Martinez, M., … Hong, S. (2020). Surface engineering for efficient capture of circulating tumor cells in renal cell carcinoma: From nanoscale analysis to clinical application. *Biosensors and Bioelectronics, 162*, 112250.

Buglione, M., Grisanti, S., Almici, C., Mangoni, M., Polli, C., Consoli, F., … Magrini, S. M. (2012). Circulating tumour cells in locally advanced head and neck cancer: Preliminary report about their possible role in predicting response to non-surgical treatment and survival. *European Journal of Cancer, 48*(16), 3019–3026.

Calderón, M., Welker, P., Licha, K., Fichtner, I., Graeser, R., Haag, R., & Kratz, F. (2011). Development of efficient acid cleavable multifunctional prodrugs derived from dendritic polyglycerol with a poly(ethylene glycol) shell. *Journal of Controlled Release, 151*(3), 295–301.

Calderón, M., Welker, P., Licha, K., Graeser, R., Kratz, F., & Haag, R. (2010). Development of efficient macromolecular prodrugs derived from dendritic polyglycerol. *Journal of Controlled Release, 148*(1), e24–e25.

Calvino, C., Macke, N., Kato, R., & Rowan, S. J. (2020). Development, processing and applications of bio-sourced cellulose nanocrystal composites. *Progress in Polymer Science, 103*, 101221.

Castner, D. G., Hinds, K., & Grainger, D. W. (1996). X-ray photoelectron spectroscopy sulfur 2p study of organic thiol and disulfide binding interactions with gold surfaces. *Langmuir, 12*(21), 5083–5086.

Chaffer, C. L., & Weinberg, R. A. (2011). A perspective on cancer cell metastasis. *Science, 331*(6024), 1559.

Chen, H., Zhang, Z., Liu, H., Zhang, Z., Lin, C., & Wang, B. (2019). *Hybrid magnetic and deformability based isolation of circulating tumor cells using microfluidics*.

Chen, W., Sun, Z., & Lu, L. (2021). Targeted engineering of medicinal chemistry for cancer therapy: Recent advances and perspectives. *Angewandte Chemie International Edition, 60*(11), 5626–5643.

Chen, X., Lin, H., Xu, T., Lai, K., Han, X., & Lin, M. (2020). Cellulose nanofibers coated with silver nanoparticles as a flexible nanocomposite for measurement of flusilazole residues in Oolong tea by surface-enhanced Raman spectroscopy. *Food Chemistry, 315*, 126276.

Cristofanilli, M., Budd, G. T., Ellis, M. J., Stopeck, A., Matera, J., Miller, M. C., … Hayes, D. F. (2004). Circulating tumor cells, disease progression, and survival in metastatic breast cancer. *New England Journal of Medicine, 351*(8), 781–791.

Czaja, W. K., Young, D. J., Kawecki, M., & Brown, R. M. (2007). The future prospects of microbial cellulose in biomedical applications. *Biomacromolecules, 8*(1), 1–12.

Deng, G., Krishnakumar, S., Powell, A. A., Zhang, H., Mindrinos, M. N., Telli, M. L., … Jeffrey, S. S. (2014). Single cell mutational analysis of PIK3CA in circulating tumor cells and metastases in breast cancer reveals heterogeneity, discordance, and mutation persistence in cultured disseminated tumor cells from bone marrow. *BMC Cancer, 14*, 456.

Descostes, M., Mercier, F., Thromat, N., Beaucaire, C., & Gautier-Soyer, M. (2000). Use of XPS in the determination of chemical environment and oxidation state of iron and sulfur samples: Constitution of a data basis in binding energies for Fe and S reference compounds and applications to the evidence of surface species of an oxidized pyrite in a carbonate medium. *Applied Surface Science, 165*(4), 288–302.

Domingues, R. M. A., Gomes, M. E., & Reis, R. L. (2014). The potential of cellulose nanocrystals in tissue engineering strategies. *Biomacromolecules, 15*(7), 2327–2346.

Dong, S., & Roman, M. (2007). Fluorescently labeled cellulose nanocrystals for bioimaging applications. *Journal of the American Chemical Society, 129*(45), 13810–13811.

Edwards, J. V., Prevost, N., French, A., Concha, M., DeLucca, A., & Wu, Q. (2013). Nanocellulose-based biosensors: Design, preparation, and activity of peptide-linked cotton cellulose nanocrystals having Fluorimetric and colorimetric elastase detection sensitivity. *Engineering, 5*(9), 20.

Fein, K., Bousfield, D. W., & Gramlich, W. M. (2020). The influence of versatile thiol-norbornene modifications to cellulose nanofibers on rheology and film properties. *Carbohydrate Polymers, 230*, 115672.

Fischer, W., Quadir, M. A., Barnard, A., Smith, D. K., & Haag, R. (2011). Controlled release of DNA from photoresponsive hyperbranched polyglycerols with oligoamine shells. *Macromolecular Bioscience, 11*(12), 1736–1746.

Fortin, J.-P., Wilhelm, C., Servais, J., Ménager, C., Bacri, J.-C., & Gazeau, F. (2007). Size-sorted anionic iron oxide nanomagnets as colloidal mediators for magnetic hyperthermia. *Journal of the American Chemical Society, 129*(9), 2628–2635.

Gatenholm, P., & Klemm, D. (2010). Bacterial nanocellulose as a renewable material for biomedical applications. *MRS Bulletin, 35*(3), 208–213.

Gipson, K., Stevens, K., Brown, P., & Ballato, J. (2015). Infrared spectroscopic characterization of photoluminescent polymer nanocomposites. *Journal of Spectroscopy, 2015*, 489162.

Gleghorn, J. P., Pratt, E. D., Denning, D., Liu, H., Bander, N. H., Tagawa, S. T., … Kirby, B. J. (2010). Capture of circulating tumor cells from whole blood of prostate cancer patients using geometrically enhanced differential immunocapture (GEDI) and a prostate-specific antibody. *Lab on a Chip, 10*(1), 27–29.

Golmohammadi, H., Morales-Narváez, E., Naghdi, T., & Merkoçi, A. (2017). *Nanocellulose in sensing and biosensing*.

Gomme, P. T., McCann, K. B., & Bertolini, J. (2005). Transferrin: Structure, function and potential therapeutic actions. *Drug Discovery Today, 10*(4), 267–273.

Han, L., Huang, R., Liu, S., Huang, S., & Jiang, C. (2010). Peptide-conjugated PAMAM for targeted doxorubicin delivery to transferrin receptor overexpressed tumors. *Molecular Pharmaceutics, 7*(6), 2156–2165.

Hazra, R. S., Dutta, D., Mamnoon, B., Nair, G., Knight, A., Mallik, S., … Quadir, M. (2021). Polymeric composite matrix with high biobased content as pharmaceutically relevant molecular encapsulation and release platform. *ACS Applied Materials & Interfaces, 13*(34), 40229–40248.

Hazra, R. S., Hasan Khan, M. R., Kale, N., Tanha, T., Khandare, J., Ganai, S., & Quadir, M. (2022). Bioinspired materials for wearable devices and point-of-care testing of cancer. *ACS Biomaterials Science & Engineering, 9*(5), 2103–2128.

Hazra, R. S., Kale, N., Aland, G., Qayyumi, B., Mitra, D., Jiang, L., … Quadir, M. (2020). Cellulose mediated transferrin nanocages for enumeration of circulating tumor cells for head and neck cancer. *Scientific Reports, 10*(1), 10010.

Hazwan Hussin, M., Trache, D., Chuin, C. T. H., Nurul Fazita, M. R., Mohamad Haafiz, M. K., & Hossain, M. S. (2019). Extraction of cellulose nanofibers and their eco-friendly polymer composites. In Inamuddin, S. Thomas, R. Kumar Mishra, & A. M. Asiri (Eds.), *Sustainable polymer composites and nanocomposites* (pp. 653–691). Cham: Springer International Publishing.

He, S., Li, P., Long, T., Zhang, N., Fang, J., & Yu, Z. (2013). Detection of circulating tumour cells with the CellSearch system in patients with advanced-stage head and neck cancer: preliminary results. *The Journal of Laryngology & Otology, 127*(8), 788–793.

Hickey, R. J., & Pelling, A. E. (2019). Cellulose biomaterials for tissue engineering. *Frontiers in Bioengineering and Biotechnology, 7*.

Hsiao, Y.-S., Luo, S.-C., Hou, S., Zhu, B., Sekine, J., Kuo, C.-W., … Chen, P. (2014). 3D bioelectronic interface: Capturing circulating tumor cells onto conducting polymer-based micro/nanorod arrays with chemical and topographical control. *Small, 10*(15), 3012–3017.

Hu, X., Zang, X., & Lv, Y. (2021). Detection of circulating tumor cells: Advances and critical concerns (review). *Oncology Letters, 21*(5).

Hussain, A. F., Krüger, H. R., Kampmeier, F., Weissbach, T., Licha, K., Kratz, F., … Barth, S. (2013). Targeted delivery of dendritic polyglycerol–doxorubicin conjugates by scFv-SNAP fusion protein suppresses EGFR+ cancer cell growth. *Biomacromolecules, 14*(8), 2510–2520.

Incani, V., Danumah, C., & Boluk, Y. (2013). Nanocomposites of nanocrystalline cellulose for enzyme immobilization. *Cellulose, 20*, 191–200.

Jia, R., Tian, W., Bai, H., Zhang, J., Wang, S., & Zhang, J. (2019). Amine-responsive cellulose-based ratiometric fluorescent materials for real-time and visual detection of shrimp and crab freshness. *Nature Communications, 10*(1), 1–8.

Jiang, X., Zhang, X., Guo, C., Yu, Y., Ma, B., Liu, Z., Chai, Y., Wang, L., Du, Y., Wang, B., Li, N., Dong, D., Li, Y., Huang, X., & Ou, L. (2022). Protein corona-coated immunomagnetic nanoparticles with enhanced isolation of circulating tumor cells. *Nanoscale, 14*(23), 8474–8483.

Jorfi, M., & Foster, E. J. (2015). Recent advances in nanocellulose for biomedical applications. *Journal of Applied Polymer Science, 132*(14).

Joseph, B., K, S. V., Sabu, C., Kalarikkal, N., & Thomas, S. (2020). Cellulose nanocomposites: Fabrication and biomedical applications. *Journal of Bioresources and Bioproducts, 5*(4), 223–237.

Kawada, T., Takahashi, H., Sakakura, K., Ida, S., Mito, I., Toyoda, M., & Chikamatsu, K. (2017). Circulating tumor cells in patients with head and neck squamous cell carcinoma: Feasibility of detection and quantitation. *Head & Neck, 39*(11), 2180–2186.

Khandare, J. J., Banerjee, S., Padigaru, M., Khutale, G., & Actorius Innovations and Research Pvt Ltd. (2016). *Multifunctional magneto-polymeric nanosystems for rapid targeting, isolation, detection and simultaneous imaging of circulating tumor cells. 2016-08-25*.

Khetani, S., Mohammadi, M., & Nezhad, A. S. (2018). Filter-based isolation, enrichment, and characterization of circulating tumor cells. *Biotechnology and Bioengineering, 115*(10), 2504–2529.

Kim, Y. B., Kim, H. K., Choi, H. C., & Hong, J. W. (2005). Photocuring of a thiol-ene system based on an unsaturated polyester. *Journal of Applied Polymer Science, 95*(2), 342–350.

Kulasinghe, A., Hughes, B. G. M., Kenny, L., & Punyadeera, C. (2019). An update: Circulating tumor cells in head and neck cancer. *Expert Review of Molecular Diagnostics, 19*(12), 1109–1115.

Kulasinghe, A., Kapeleris, J., Kimberley, R., Mattarollo, S. R., Thompson, E. W., Thiery, J.-P., … Punyadeera, C. (2018). The prognostic significance of circulating tumor cells in head and neck and non-small-cell lung cancer. *Cancer Medicine, 7*(12), 5910–5919.

Kulasinghe, A., Kenny, L., Perry, C., Thiery, J.-P., Jovanovic, L., Vela, I., Nelson, C., & Punyadeera, C. (2016). Impact of label-free technologies in head and neck cancer circulating tumour cells. *Oncotarget, 7*(44), 71223–71234.

Kulasinghe, A., Perry, C., Jovanovic, L., Nelson, C., & Punyadeera, C. (2015). Circulating tumour cells in metastatic head and neck cancers. *International Journal of Cancer, 136*(11), 2515–2523.

Kulasinghe, A., Perry, C., Kenny, L., Warkiani, M. E., Nelson, C., & Punyadeera, C. (2017). PD-L1 expressing circulating tumour cells in head and neck cancers. *BMC Cancer, 17*(1), 1–6.

Kulasinghe, A., Zhou, J., Kenny, L., Papautsky, I., & Punyadeera, C. (2019). Capture of circulating tumour cell clusters using straight microfluidic chips. *Cancers (Online), 11*(1), 89.

Kumar, T., Soares, R. R. G., Ali Dholey, L., Ramachandraiah, H., Aval, N. A., Aljadi, Z., … Russom, A. (2020). Multi-layer assembly of cellulose nanofibrils in a microfluidic device for the selective capture and release of viable tumor cells from whole blood. *Nanoscale, 12*(42), 21788–21797.

Lam, E., Male, K. B., Chong, J. H., Leung, A. C., & Luong, J. H. (2012). Applications of functionalized and nanoparticle-modified nanocrystalline cellulose. *Trends in Biotechnology, 30*(5), 283–290.

Lee, A.-W., Lin, F.-X., Wei, P.-L., Jian-Wei, G., & Chen, J.-K. (2018). Binary-blend fibber-based capture assay of circulating tumor cells for clinical diagnosis of colorectal cancer. *Journal of Nanobiotechnology, 16*(1), 1–16.

Lee, S. J., Sim, T. S., Shin, H. Y., Lee, J., Kim, M. Y., Sunoo, J., … Kim, M. S. (2019). Microslit on a chip: A simplified filter to capture circulating tumor cells enlarged with microbeads. *PLoS One, 14*(10), Article e0223193.

Li, C., Li, R., Wu, X., Zuo, Y., Xiong, G., Huang, M., … Yu, Y. (2022). Capture of heterogeneous circulating tumor cells in colorectal cancer patients on an immunomagnetic and anti-nonspecific adsorption platform. *Analytical Chemistry, 94*(44), 15240–15249.

Li, G., Shang, Y., Wang, Y., Wang, L., Chao, Y., & Qi, Y. (2019). Reaction mechanism of etherification of rice straw with epichlorohydrin in alkaline medium. *Scientific Reports, 9*(1), 14307.

Li, K., Skolrood, L. N., Aytug, T., Tekinalp, H., & Ozcan, S. (2019). Strong and tough cellulose nanofibrils composite films: Mechanism of synergetic effect of hydrogen bonds and ionic interactions. *ACS Sustainable Chemistry & Engineering, 7*(17), 14341–14346.

Li, Y., Wu, S., & Bai, F. (2018). Molecular characterization of circulating tumor cells—From bench to bedside. *Seminars in Cell & Developmental Biology, 75*, 88–97.

Lin, N., & Dufresne, A. (2013). Supramolecular hydrogels from in situ host–guest inclusion between chemically modified cellulose nanocrystals and cyclodextrin. *Biomacromolecules, 14*(3), 871–880.

Liu, Y., Cheng, Y., Zhao, C., Wang, H., & Zhao, Y. (2022). Nanomotor-derived porous biomedical particles from droplet microfluidics. *Advanced Science, 9*(4), 2104272.

Lu, N.-N., Xie, M., Wang, J., Lv, S.-W., Yi, J.-S., Dong, W.-G., & Huang, W.-H. (2015). *Biotin-triggered decomposable immunomagnetic beads for capture and release of circulating tumor cells*.

Luan, C., Wang, H., Han, Q., Ma, X., Zhang, D., Xu, Y., … Zhao, Y. (2018). Folic acid-functionalized hybrid photonic barcodes for capture and release of circulating tumor cells. *ACS Applied Materials & Interfaces, 10*(25), 21206–21212.

Ma, Q., Wang, K., Mohawk, D., Chen, Y., Hazra, R., & Jiang, L. (2021). Strong, ductile, transparent, water-resistant cellulose nanofibril composite films via UV-induced inter-cross-linked networks. *ACS Sustainable Chemistry & Engineering, 9*(32), 10749–10760.

Mahmoud, K. A., Mena, J. A., Male, K. B., Hrapovic, S., Kamen, A., & Luong, J. H. (2010). Effect of surface charge on the cellular uptake and cytotoxicity of fluorescent labeled cellulose nanocrystals. *ACS Applied Materials & Interfaces, 2*(10), 2924–2932.

McMullen Kyle, P., Chalmers Jeffrey, J., Lang Jas, C., Kumar, P., Jatana Kris, R., & Gao, J. (2016). Circulating tumor cells in head and neck cancer: A review. *World Journal of Otorhinolaryngology - Head and Neck Surgery, 02*(02), 109–116.

Meng, S., Tripathy, D., Frenkel, E. P., Shete, S., Naftalis, E. Z., Huth, J. F., … Uhr, J. W. (2004). Circulating tumor cells in patients with breast cancer dormancy. *Clinical Cancer Research, 10*(24), 8152.

Meng, X., Sun, P., Xu, H., & Wang, Z. (2020). Folic acid-functionalized magnetic nanoprobes via a PAMAM dendrimer/SA-biotin mediated cascade-amplifying system for the efficient enrichment of circulating tumor cells. *Biomaterials Science, 8*(22), 6395–6403.

Montanari, C., Ogawa, Y., Olsén, P., & Berglund, L. A. (2021). High performance, fully bio-based, and optically transparent wood biocomposites. *Advanced Science, 8*(12), 2100559. https://doi.org/10.1002/advs.202100559

Myung, J. H., Gajjar, K. A., Han, Y. E., & Hong, S. (2012). The role of polymers in detection and isolation of circulating tumor cells. *Polymer Chemistry, 3*(9), 2336.

Myung, J. H., Gajjar, K. A., Saric, J., Eddington, D. T., & Hong, S. (2011). Dendrimer-mediated multivalent binding for the enhanced capture of tumor cells. *Angewandte Chemie, 123*(49), 11973–11976.

Myung, J. H., Roengvoraphoj, M., Tam, K. A., Ma, T., Memoli, V. A., Dmitrovsky, E., … Hong, S. (2015). Effective capture of circulating tumor cells from a transgenic mouse lung cancer model using dendrimer surfaces immobilized with anti-EGFR. *Analytical Chemistry, 87*(19), 10096–10102.

Nagrath, S., Sequist, L. V., Maheswaran, S., Bell, D. W., Irimia, D., Ulkus, L., … Toner, M. (2007). Isolation of rare circulating tumour cells in cancer patients by microchip technology. *Nature, 450*(7173), 1235–1239.

Necula, L., Matei, L., Dragu, D., Neagu, A. I., Mambet, C., Nedeianu, S., … Chivu-Economescu, M. (2019). Recent advances in gastric cancer early diagnosis. *World Journal of Gastroenterology, 25*(17), 2029–2044.

Nichols, A. C., Lowes, L. E., Szeto, C. C. T., Basmaji, J., Dhaliwal, S., Chapeskie, C., … Allan, A. L. (2012). Detection of circulating tumor cells in advanced head and neck cancer using the cellsearch system. *Head & Neck, 34*(10), 1440–1444.

Noel, S., Liberelle, B., Robitaille, L., & De Crescenzo, G. (2011). Quantification of primary amine groups available for subsequent biofunctionalization of polymer surfaces. *Bioconjugate Chemistry, 22*(8), 1690–1699.

Omran, M., Fabritius, T., Elmahdy, A. M., Abdel-Khalek, N. A., El-Aref, M., & Elmanawi, A. E.-H. (2015). XPS and FTIR spectroscopic study on microwave treated high phosphorus iron ore. *Applied Surface Science, 345*, 127–140.

Ottenhall, A., Seppänen, T., & Ek, M. (2018). Water-stable cellulose fiber foam with antimicrobial properties for bio based low-density materials. *Cellulose, 25*(4), 2599–2613.

Pennells, J., Godwin, I. D., Amiralian, N., & Martin, D. J. (2020). Trends in the production of cellulose nanofibers from non-wood sources. *Cellulose, 27*(2), 575–593.

Picheth, G. F., Pirich, C. L., Sierakowski, M. R., Woehl, M. A., Sakakibara, C. N., de Souza, C. F., … de Freitas, R. A. (2017). Bacterial cellulose in biomedical applications: A review. *International Journal of Biological Macromolecules, 104*, 97–106.

Porath, I., & Fornstedt, N. (1970). Group fractionation of plasma proteins on dipolar ion exchangers. *Journal of Chromatography A, 51*, 479–489.

Postek, M. T., Moon, R. J., Rudie, A. W., & Bilodeau, M. A. (2013). *Production and applications of cellulose nanomaterials*. TAPPI Press (Order number: 0101R332; ISBN: 978-1-59510-224-9).

Prathapan, R., Thapa, R., Garnier, G., & Tabor, R. F. (2016). Modulating the zeta potential of cellulose nanocrystals using salts and surfactants. *Colloids and Surfaces A: Physicochemical and Engineering Aspects, 509*, 11–18.

Rakib Hasan Khan, M., Shankar Hazra, R., Nair, G., Mohammad, J., Jiang, L., Reindl, K., Khalid Jawed, M., Ganai, S., & Quadir, M. (2022). Cellulose nanofibers as scaffold-forming materials for thin film drug delivery systems. *International Journal of Pharmaceutics*, 122189.

Rose, M., & Palkovits, R. (2011). Cellulose-based sustainable polymers: State of the art and future trends. *Macromolecular Rapid Communications, 32*(17), 1299–1311.

Schulz, M. J., Shanov, V. N., & Yun, Y. (2009). Nanomedicine design of particles, sensors, motors, implants, robots, and devices. In *Artech House series engineering in medicine & biology*.

Shen, Z., Wu, A., & Chen, X. (2017). Current detection technologies for circulating tumor cells. *Chemical Society Reviews, 46*(8), 2038–2056.

Singh, B., Arora, S., D'Souza, A., Kale, N., Aland, G., Bharde, A., … Khandare, J. (2021). Chemo-specific designs for the enumeration of circulating tumor cells: Advances in liquid biopsy. *Journal of Materials Chemistry B, 9*(13), 2946–2978.

Sun, N., Li, X., Wang, Z., Li, Y., & Pei, R. (2018). High-purity capture of CTCs based on micro-beads enhanced isolation by size of epithelial tumor cells (ISET) method. *Biosensors and Bioelectronics, 102*, 157–163.

Sung, H., Ferlay, J., Siegel, R. L., Laversanne, M., Soerjomataram, I., Jemal, A., & Bray, F. (2021). Global cancer statistics 2020: GLOBOCAN estimates of incidence and mortality worldwide for 36 cancers in 185 countries. *CA: A Cancer Journal for Clinicians, 71*(3), 209–249.

Tada, H., Takahashi, H., Kuwabara-Yokobori, Y., Shino, M., & Chikamatsu, K. (2020). Molecular profiling of circulating tumor cells predicts clinical outcome in head and neck squamous cell carcinoma. *Oral Oncology, 102*, 104558.

Talasaz, A. H., Powell, A. A., Huber, D. E., Berbee, J. G., Roh, K.-H., Yu, W., … Davis, R. W. (2009). *Isolating highly enriched populations of circulating epithelial cells and other rare cells from blood using a magnetic sweeper device*.

Talasaz, A. H., Powell, A. A., Stahl, P., Ronaghi, M., Jeffrey, S. S., Mindrinos, M., & Davis, R. W. (2006). Cell trapping in activated micropores for functional analysis. *Conference Proceedings: Annual International Conference of the IEEE Engineering in Medicine and Biology Society, 1*, 1838–1841.

Tayoun, T., Faugeroux, V., Oulhen, M., Aberlenc, A., Pawlikowska, P., & Farace, F. (2019). CTC-derived models: A window into the seeding capacity of circulating tumor cells (CTCs). *Cells, 8*(10).

Tinhofer, I., & Staudte, S. (2018). Circulating tumor cells as biomarkers in head and neck cancer: Recent advances and future outlook. *Expert Review of Molecular Diagnostics, 18*(10), 897–906.

Trache, D., Khimeche, K., Mezroua, A., & Benziane, M. (2016). Physicochemical properties of microcrystalline nitrocellulose from Alfa grass fibres and its thermal stability. *Journal of Thermal Analysis and Calorimetry, 124*(3), 1485–1496.

Trache, D., Tarchoun, A. F., Derradji, M., Hamidon, T. S., Masruchin, N., Brosse, N., & Hussin, M. H. (2020). Nanocellulose: From fundamentals to advanced applications. *Frontiers in Chemistry, 8*.

Tseng, H.-C., Lee, A.-W., Wei, P.-L., Chang, Y.-J., & Chen, J.-K. (2016). Clinical diagnosis of colorectal cancer using electrospun triple-blend fibrous mat-based capture assay of circulating tumor cells. *Journal of Materials Chemistry B, 4*(40), 6565–6580.

Unal, S., Gunduz, O., & Uzun, M. (2020). Tissue engineering applications of bacterial cellulose based nanofibers. In S. Ahmed, & W. Ali (Eds.), *Green nanomaterials: Processing, properties, and applications* (pp. 319–346). Singapore: Springer Singapore.

Wang, L., Chen, C., Wang, J., Gardner, D. J., & Tajvidi, M. (2020). Cellulose nanofibrils versus cellulose nanocrystals: Comparison of performance in flexible multilayer films for packaging applications. *Food Packaging and Shelf Life, 23*, 100464.

Wu, L., Zhu, L., Huang, M., Song, J., Zhang, H., Song, Y., Wang, W., & Yang, C. (2019). Aptamer-based microfluidics for isolation, release and analysis of circulating tumor cells. *TrAC Trends in Analytical Chemistry, 117*, 69–77.

Xiong, K., Wei, W., Jin, Y., Wang, S., Zhao, D., Gao, X., … Xie, H. Y. (2016). Biomimetic immuno-magnetosomes for high-performance enrichment of circulating tumor cells. *Advanced Materials, 28*(36), 7929–7935.

Xu, R. (2001). *Particle characterization: Light scattering methods*. Dordrecht: Kluwer Academic Publishers.

Xu, X., Liu, F., Jiang, L., Zhu, J., Haagenson, D., & Wiesenborn, D. P. (2013). Cellulose nanocrystals vs. cellulose nanofibrils: A comparative study on their microstructures and effects as polymer reinforcing agents. *ACS Applied Materials & Interfaces, 5*(8), 2999–3009.

Yoo, C. E., Moon, H. S., Kim, Y. J., Park, J. M., Park, D., Han, K. Y., … Park, W. Y. (2016). Highly dense, optically inactive silica microbeads for the isolation and identification of circulating tumor cells. *Biomaterials, 75*, 271–278.

Yoon, H. J., Shanker, A., Wang, Y., Kozminsky, M., Jin, Q., Palanisamy, N., … Nagrath, S. (2016). Tunable thermal-sensitive polymer-graphene oxide composite for efficient capture and release of viable circulating tumor cells. *Advanced Materials, 28*(24), 4891–4897.

Zhang, L., Li, Q., Zhou, J., & Zhang, L. (2012). Synthesis and photophysical behavior of pyrene-bearing cellulose nanocrystals for Fe3+ sensing. *Macromolecular Chemistry and Physics, 213*(15), 1612–1617.

Zhang, W., Wang, J., Li, P., Wu, C., Zhang, H., Zhang, W., … Tang, B. (2017). Transferrin-navigation nano artificial antibody fluorescence recognition of circulating tumor cells. *Scientific Reports, 7*(1), 1–10.

Zhang, Z., & King, M. R. (2017). Nanomaterials for the capture and therapeutic targeting of circulating tumor cells. *Cellular and Molecular Bioengineering, 10*(4), 275–294.

Zhao, K., Zhao, P., Dong, J., Wei, Y., Chen, B., Wang, Y., … Wang, J. (2022). Implementation of an integrated dielectrophoretic and magnetophoretic microfluidic chip for CTC isolation. *Biosensors, 12*(9), 757.

Zheng, F., Cheng, Y., Wang, J., Lu, J., Zhang, B., Zhao, Y., & Gu, Z. (2014). Aptamer-functionalized barcode particles for the capture and detection of multiple types of circulating tumor cells. *Advanced Materials, 26*(43), 7333–7338.

Zheng, S., Lin, H. K., Lu, B., Williams, A., Datar, R., Cote, R. J., & Tai, Y.-C. (2011). 3D microfilter device for viable circulating tumor cell (CTC) enrichment from blood. *Biomedical Microdevices, 13*(1), 203–213.

Zheng, W., Zhang, Y., Guo, L., Wang, S., Fang, M., Mao, W., & Lou, J. (2019). Evaluation of therapeutic efficacy with CytoSorter(®) circulating tumor cell-capture system in patients with locally advanced head and neck squamous cell carcinoma. *Cancer Management and Research, 11*, 5857–5869.

Zhu, L., Shao, C., Chen, H., Chen, Z., & Zhao, Y. (2021). Hierarchical hydrogels with ordered micro-nano structures for cancer-on-a-chip construction. *Research, 2021*.